ELSEVIER

Nuclear Engineering and Design 189 (1999) 103–138

Nuclear Engineering and Design

The verification basis of the ESPROSE.m code

T.G. Theofanous *, W.W. Yuen, K. Freeman, X. Chen

Center for Risk Studies and Safety, University of California, Santa Barbara, Santa Barbara, CA 93106, USA

Received 24 August 1998; accepted 24 November 1998

Abstract

An overall verification approach for the ESPROSE.m code is presented and implemented. The approach consists of a stepwise testing procedure from wave dynamics aspects to explosion coupling at the local level, and culminates with the consideration of propagating explosive events. Each step in turn consists of an array of analytical and experimental tests. The results indicate that, given the premixture composition, the prediction of energetics of large scale explosions in multidimensional geometries is within reach. The main need identified is for constitutive laws for microinteractions with reactor materials; however, reasonably conservative assessments are presently possible.

Keywords: ESPROSE.m; Steam explosions; Multiphase thermal detonations; Microinteractions; Computational fluid dynamics; Multiphase flow

1. Introduction

The purpose of this paper is to present a verification statement supporting the use of the computer code ESPROSE.m in assessing the propagation of steam explosions in reactor geometries and conditions. Our specific interest is in obtaining reasonably conservative results on explosion energetics and damage potential, so as to be of use in safety analyses, and for licensing purposes as well. The overall approach has been described previously (Theofanous et al., 1995a). It involves a methodology (Theofanous, 1996) and a set of codes, as illustrated in Table 1. The codes are supported by respective verification documents, and the approach is exemplified by the first application, as also noted in Table 1. The present paper is one (DOE/ID-10503) of this suite of documents, and it should be studied in this context, as part of a whole. Most necessary in this respect is the description of the modeling approach and mathematical formulation of ESPROSE.m. They can be found in DOE/ID-10503. In the same vein, a familiarization with Theofanous et al. (1995a) is highly recommended, prior to delving in the present details.

The structural outline of our verification approach is illustrated in Fig. 1. It provides a systematic frame for the verification task, and thus a means to conclusion in this inherently open-ended

* Corresponding author. Tel.: +1-805-893-4900; fax: +1-805-893-4927.

E-mail address: theo@theo.ucsb.edu (T.G. Theofanous)

0029-5493/99/$ - see front matter
PII: S0029-5493(99)00030-8

endeavor. The same figure, keyed to sections and subsections, also serves to guide the reader through the wide variety of topics in this document. The nomenclature is explained as it is used and, to the extent possible, it is made consistent among sections. As the various elements in this figure are self explanatory, we defer all explanations to the respective topic. From a top-level perspective the 'wave dynamics' and 'explosion coupling' will be recognized as the key ingredients (or fundamental components) of the explosion physics, as explained in Appendix A of Theofanous et al. (1995b). The integral aspects are very important here, because, if properly satisfied in terms of a soundly-based (consistent) treatment of the two fundamental components, in 1D problems, the applicability to 2D (or 3D) situations follows as a consequence of having verified the wave dynamics aspects in such multidimensional geometries.

Table 1
Steam explosion energetics and structural damage potential

Introductory and overall approach		The study—DOE/ID-10489[a]
Topical element	Codes	Documents
Initial conditions	Special purpose models	In-vessel SE: DOE/ID-10505[b] Ex-vessel SE: DOE/ID-10506[c]
Premixing	PM-ALPHA	Manual: DOE/ID-10502[d] Verification: DOE/ID-10504[e]
	THIRMAL	Manual: EPRITR-103417[f]
Propagation	ESPROSE.m	Manual: DOE/ID-10501[g] Verification: DOE/ID-10503[h]
Structural response	ANACAP-3D/ABAQUS	Manual[i] Verification: ANA-89-0094[j]
Integration/application		In-vessel SE: DOE/ID-10505[b] Ex-vessel SE: DOE/ID-10506[c]

[a] Theofanous et al. (1995a).
[b] Theofanous et al.a.
[c] Theofanous et al.b; the SBWR was discontinued.
[d] Yuen and Theofanous (1995b).
[e] Theofanous et al. (1995c)
[f] THIRMAL-1, (1993)
[g] Yuen and Theofanous (1995a)
[h] Theofanous et al. (1995b)
[i] Hibbit et al., (1994)
[j] James (1989)

All calculations in this paper have been done with the models described in Appendix A of Theofanous et al. (1995b), implemented in the original 2D version of the code named ESPROSE.m. We now have a 3D code also, using the same models, but based on a largely different numerical scheme. This code, called ESPROSE.m-3D, has been verified at this point by comparison to ESPROSE.m in 1D and 2D problems, as discussed in Section 4 (2D/3D code comparisons).

2. Wave dynamics

The purpose of this section is to test the ESPROSE.m code on its ability to handle pressure waves in single and multiphase media, in 1D and 2D geometries. Of particular interest are the reflection/transmission behaviors at sharp interphases of media with different acoustic impedances, and the coupling of this behavior with the energy release in an explosion. On more mundane grounds, it is important to ensure that the numerical scheme properly captures shocks, without excessive dispersion, and that wave speeds are accurately computed over the whole range of void fractions. An array of analytical and experimental tests have been devised for these purposes, as explained below.

2.1. Analytical tests

2.1.1. Exact and characteristics solutions in 1D geometries

Here we consider shock-tube-type problems, as illustrated in Fig. 2, and reference solutions obtained in closed form or with the code CHAT, described in Appendix B of Theofanous et al. (1995b).

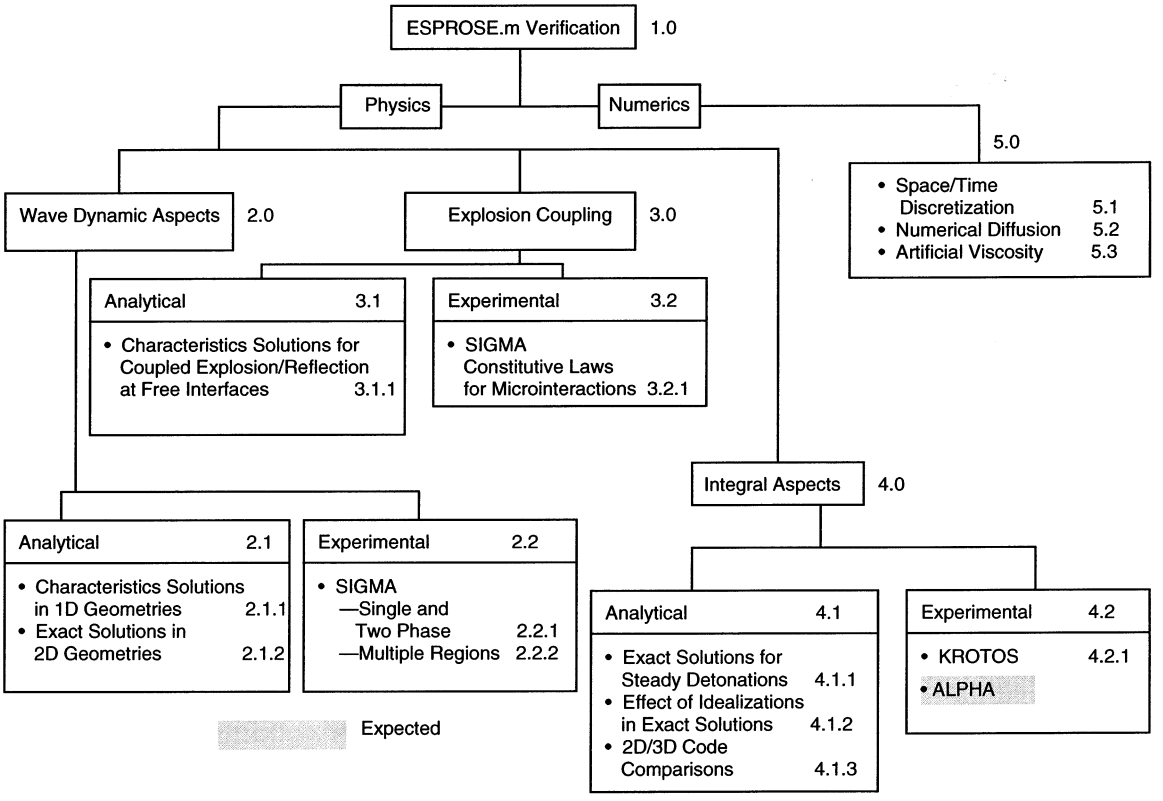

Fig. 1. Overview of the ESPROSE.m verification effort and guide through the paper.

A number of cases were considered as summarized in Table 2. The closed-form solutions indicated in this table are given below. The liquid sound speed is assumed to be constant in the derivation of these equations. For nomenclature, see Fig. 2.

- Single phase

$$c = a\sqrt{\frac{\rho_2}{\rho_1}} \tag{1}$$

$$u_2 = \frac{p_2 - p_1}{\rho_1 c} \tag{2}$$

$$c_r = a\sqrt{\frac{\rho_2}{\rho_3}} \tag{3}$$

$$p_3 - p_1 = (p_2 - p_1)\left[1 + \sqrt{\frac{\rho_3}{\rho_1}}\right] \tag{4}$$

- Two-phase, homogeneous equilibrium model

$$c_2 = \frac{\rho_2}{\rho_1}\left[\frac{1}{\frac{1}{a_1^2} + \frac{\alpha(\rho_{l,1} - \rho_{g,1})}{p_2 - p_1}}\right] \tag{5}$$

$$u_2 = \frac{p_2 - p_1}{\rho_1 c} \tag{6}$$

$$c_r = a_1\sqrt{\frac{\rho_2}{\rho_3}} \tag{7}$$

$$p_3 - p_2 = \rho_2 c_r u_2 \tag{8}$$

In the above equations, the subscripts 1 and 2 stand for initial properties evaluated ahead of the shock and behind the shock, respectively. The subscript 3 stands for properties evaluated behind the shock after its reflection off the solid wall, c_r is the reflected shock speed, α is the void fraction, and ρ_l and p_g are densities of the liquid and gas phase, respectively. The table also shows where, in the figures, the various comparisons can be found. Where appropriate, node sizes and time steps are shown in the captions (Figs. 3–10).

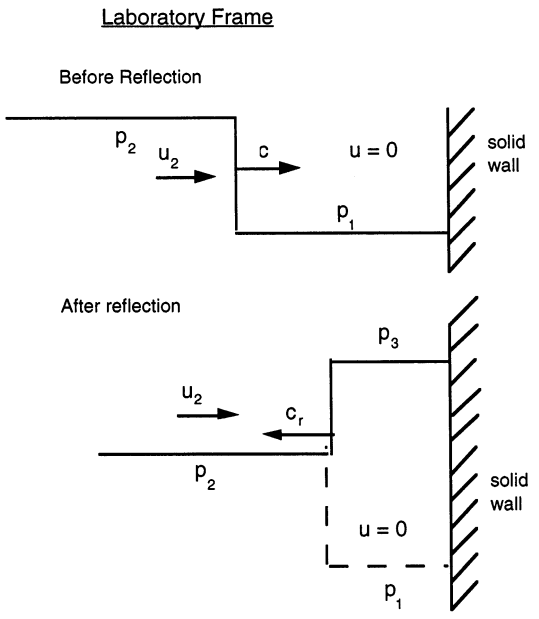

Fig. 2. Geometry and notations used for the analytical solution of a one-dimensional shock reflecting off a solid wall (Eqs. (1)–(8)).

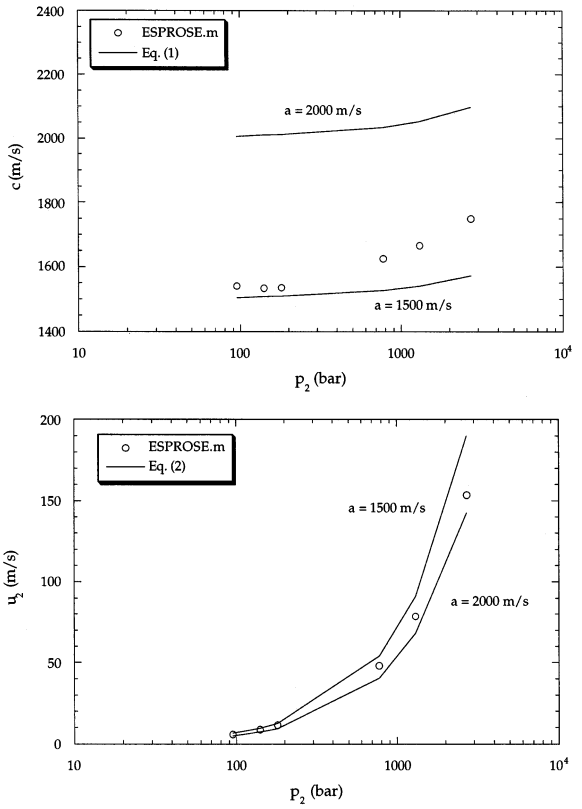

Fig. 3. Comparison between ESPROSE.m and analytical prediction of shock speed and liquid velocity based on Eqs. (1) and (2). (Analytical solutions are evaluated based on constant sound speed of 1500 and 2000 m/s. p_1 is set to be 1 bar. Real properties of water are used in the ESPROSE.m calculations.)

2.1.2. Exact solutions in 2D geometries

The interest in these types of geometries arises from steam explosions in large open pools, as illustrated in Fig. 11. The explosion zone radiates pressure waves and one would like to know the resulting loading at the bottom and side boundaries. Depending on the aspect ratio (H/R_p) reflection off the free surface (venting) can significantly influence the results (Theofanous and Yuen, 1994), and the accurate numerical treatment of these reflections is the principal objective of this portion of the verification effort. In addition, it is important to verify the 2D wave propa-

Table 2
Summary of test cases for 1D wave dynamics

	Single phase	Liquid–air (homogeneous)	Liquid–vapor (homogeneous-equilibrium)
Shock speed (c) and fluid velocity (u_2)	ESPROSE.m vs. Eqs. (1) and (2) (Fig. 3)	ESPROSE.m vs. CHAT[a] (Fig. 8)	ESPROSE.m vs. Eqs. (5) and (6) (Fig. 5)
Reflection at a rigid wall, (c_r, p_3)	ESPROSE.m vs. Eqs. (3) and (4) (Fig. 4)	ESPROSE.m vs. CHAT[a] (Fig. 9)	ESPROSE.m vs. Eqs. (7) and (8) (Fig. 6)
Reflection at a free interface and venting (c_r, p_3)	ESPROSE.m vs. CHAT[a] (Fig. 7)	ESPROSE.m vs. CHAT[a] (Fig. 10)	

[a] CHAT solves the linearized mass, momentum and energy equation, for a homogeneous gas–liquid mixture using the method of characteristics.

gation characteristics of the code, especially in relation to capturing the shock front.

For liquids, the acoustic approximation (constant speed of sound) is accurate into the kilobar range, the conservation equations can be linearized, and different kinds of wave forms can be analytically generated by introducing an appropriate mass inflow history, at the origin (see for example Moody, 1990). These wave forms are further 'tailored' due to reflections, at the interfaces, which can be accounted for by superposing elementary solutions from appropriately placed sources and/or sinks. The end results are exact, closed-form, solutions against which ESPROSE.m results can be compared. These ESPROSE.m simulations were obtained by programming an appropriate mass source over an approximately spherical domain at the origin.

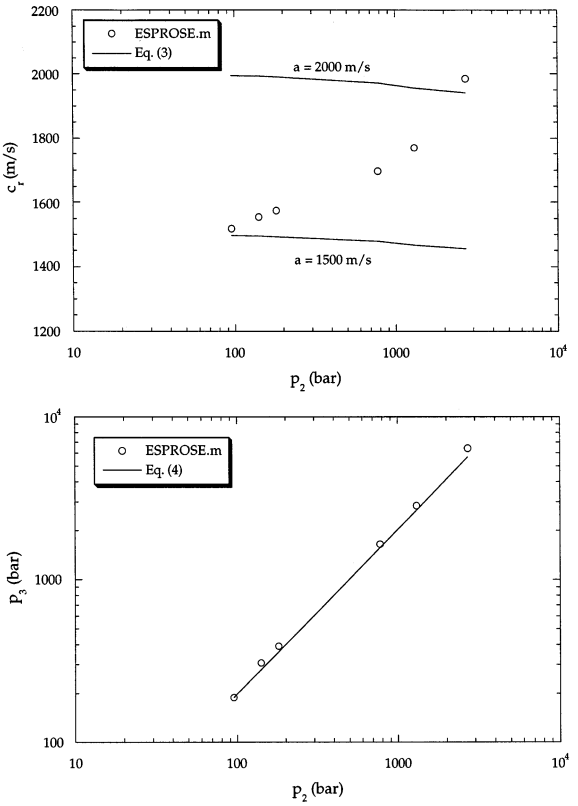

Fig. 4. Comparison between ESPROSE.m and analytical prediction of the reflected shock speed and reflected shock amplitude based on Eqs. (3) and (4). (Analytical solutions are evaluated based on a constant sound speed of 1500 m/s. p_1 is set to be 1 bar. Results for reflected shock speed with sound speed of 2000 m/s are also presented. Real properties are used in the ESPROSE.m calculations.)

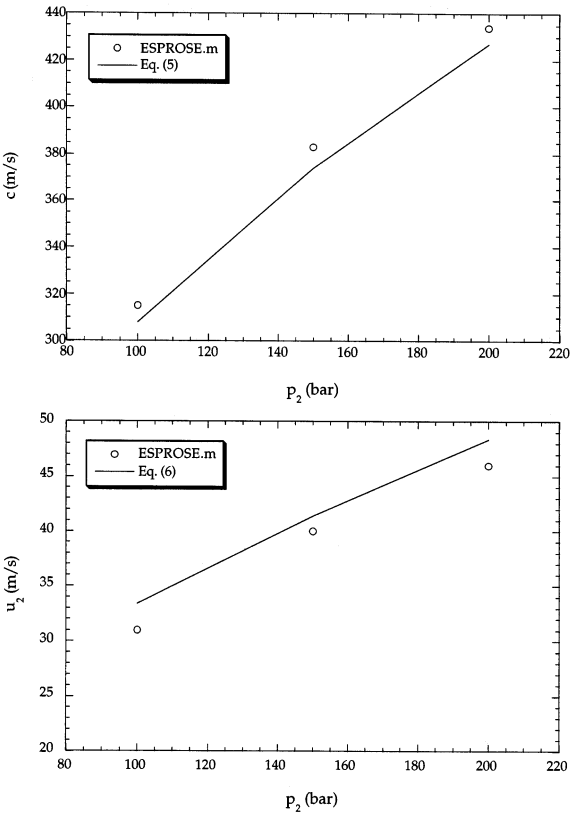

Fig. 5. Comparison between ESPROSE.m and analytical prediction of shock speed and liquid velocity based on Eqs. (5) and (6), for a 10% void steam/water mixture. (Analytical solutions are evaluated based on a constant liquid sound speed of 1500 m/s. p_1 is set to be 1 bar. Real properties are used in the ESPROSE.m calculations.)

Two source strength histories and three geometries were considered, as indicated in Table 3. Source type A maintains a high pressure at the origin, while under source type B the pressure at the origin decays after time t_0, thus creating an outwards moving wave-packet. The elementary solutions, valid for infinite media, are shown in Table 4.

The solutions for cylindrical pools can be obtained from these elementary solutions by superposition, as illustrated in Figs. 12 and 13. That is, a rigid boundary receiving a compression wave

from a given source can be represented by superposing a source of equal strength at a mirror image location with respect to the boundary. For a free interface, or for a rarefaction wave reaching a rigid boundary, the image must be a sink. On the other hand, a source is needed when a rarefaction wave hits a free surface. Depending on the aspect ratio (H/R_p) there may be multiple reflections before the wave front reaches the outer, radial boundary (at which time this method of solution cannot be continued), and a corresponding number of sources and/or sinks must then be superposed. The computation can be conveniently programmed on the computer. A full comparison between ESPROSE.m and the analytical solution (over the full transient of the propagation) is presented in Theofanous et al. (1995b). Some typical results are shown in figures as indicated in Table 3. Each figure also contains node size and time step information on the ESPROSE.m calculation (Figs. 14–17).

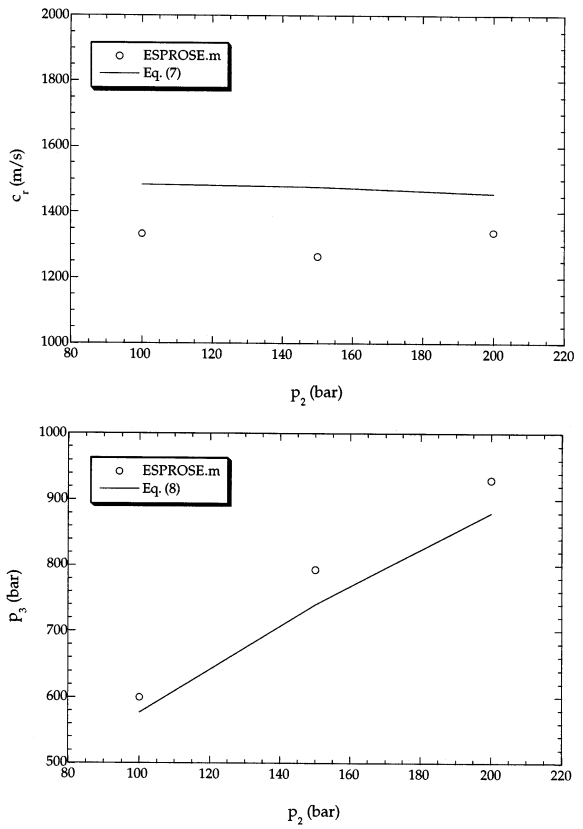

Fig. 6. Comparison between ESPROSE.m and analytical prediction of the reflected shock speed and reflected shock amplitude based on Eqs. (7) and (8), for a 10% void steam/water mixture. (Analytical solutions are evaluated based on a constant liquid sound speed of 1500 m/s. P_1 is set to 1 bar. Real properties are used in the ESPROSE.m calculations.)

Remarkable in these results are the soliton-like solutions obtained with source type B. This type of behavior in shallow open pools (Fig. 15) was initially observed in actual ESPROSE.m calculations for steam explosions, and its counter-intuitive nature led to this portion of the verification program.

2.2. Experimental tests

Here, we present comparisons with experimentally obtained pressure waves in the SIGMA facility. To our knowledge, these are the only available data for high amplitude waves, (kpsi, or hundreds of bar range) in multiphase media.

The SIGMA facility is a hydrodynamic shock tube. It was initially built to study the hydrodynamic fragmentation of drops, and more recently it has been utilized for the study of microinteractions in exploding melt drops under simulated, large-scale explosion conditions (see Section 3.2.1). A detailed description of the facility can be found in Theofanous et al. (1995a).

A schematic of the SIGMA facility relevant to our purposes here is provided in Fig. 18. A shock wave is created by rupturing the diaphragm that separates the driver from the expansion section. The pressure waves generated are measured at two locations, allowing the precise determination of the wave speed through the intervening medium. Perhaps more importantly, these measurements reveal overall complex wave dynamics with subsequent reflections at the top and bottom rigid boundaries, the interface between the two media in the driver and expansion sections, and any other interfaces purposely created in the expansion section by the placement of voids. These void fraction regions could be precisely 'tailored' to any desired axial shape and bubble size, by using air trapped inside thin plastic sheets, as used for packing material. We have also used ping pong balls.

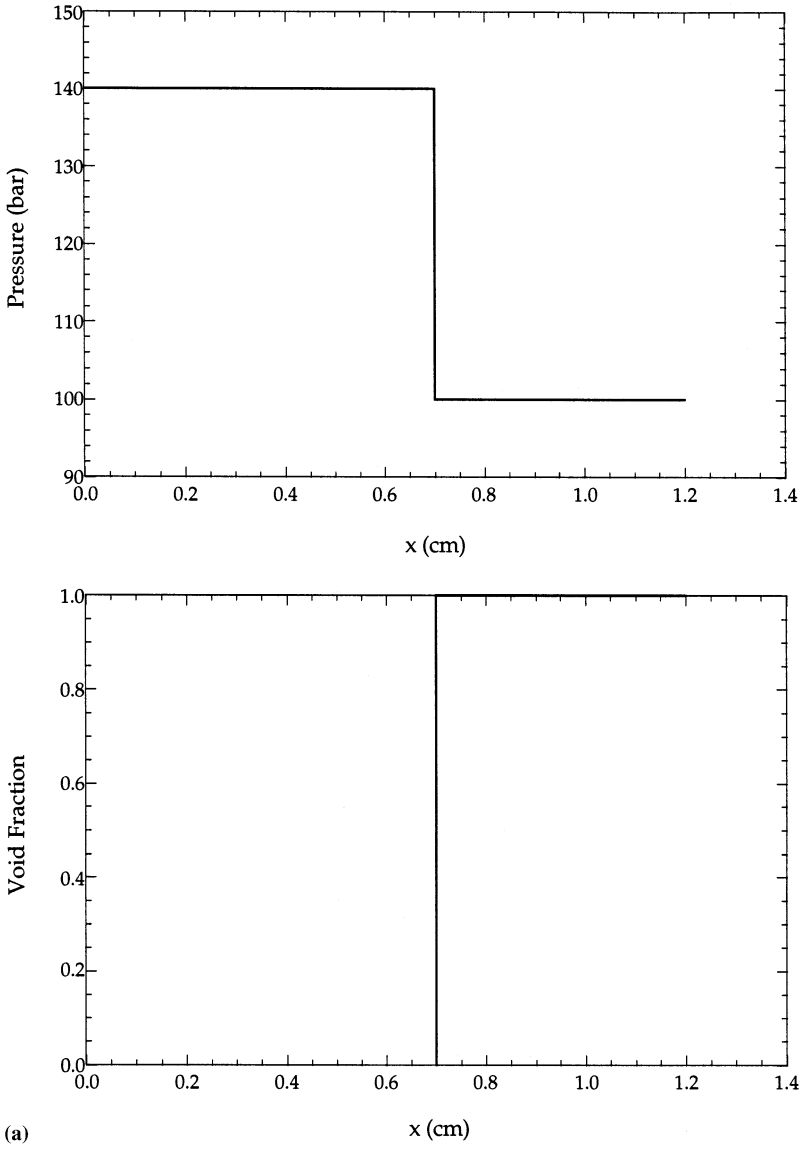

Fig. 7. (a) Initial pressure and void distribution used in the ESPROSE.m/CHAT comparison on single phase venting at a free surface.

The window allows direct visualization of the fluid, its velocity can be measured by the motion of neutral tracers captured by the flow, and the collapse and/or fragmentation of a second phase also can be directly observed.

Besides their value for verification purposes, these data are needed to clearly establish the fragmentation environment in the microinteractions studies, and, moreover, they are important in revealing the internal structure of steam explosions (coupling wave front to fragmentation kinetics).

The results are plotted in absolute rather than pressure ratios, as the former is of more direct interest here.

2.2.1. Single and two-phase SIGMA results

For a single liquid (water) in the expansion section, a sharp, step-like rise in pressure was obtained by minimizing the opening time of diaphragms (appropriate design, diaphragm parameters tailored to each pressure level). This, of course, was more than adequate under two-phase conditions.

Typical pressure traces for water are shown, together with ESPROSE.m simulations, in Fig. 19. These figures also show the reflected waves from the shock tube bottom (rigid), and internal reflections at the gas–liquid interface.

Typical pressure traces under two-phase conditions are shown together with ESPROSE.m results in Fig. 20. The experimental conditions from 12 runs, and respective results, including ESPROSE.m simulations and analytical predictions (homogeneous isothermal), are summarized in Table 5. The comparison of results in graphical form is shown in Fig. 21. The case of an extremely inhomogeneous two-phase mixture (the PPB run) is seen to deviate significantly. The pressure traces for this case (Fig. 22) shows discrete collapsing events, but it is interesting that on the average, and especially the reflection, are captured reasonably well. A collapse event in the run Bubble IX (with thin plastic sheet 'bubble') is shown in Fig. 23.

2.2.2. Multiregion SIGMA results

A series of runs were carried out in SIGMA with an axial void fraction distribution of the shape shown in Fig. 24, and void fractions in the two-phase region, corresponding to some of the runs in Table 5 of Section 2.2.1. Interesting wave

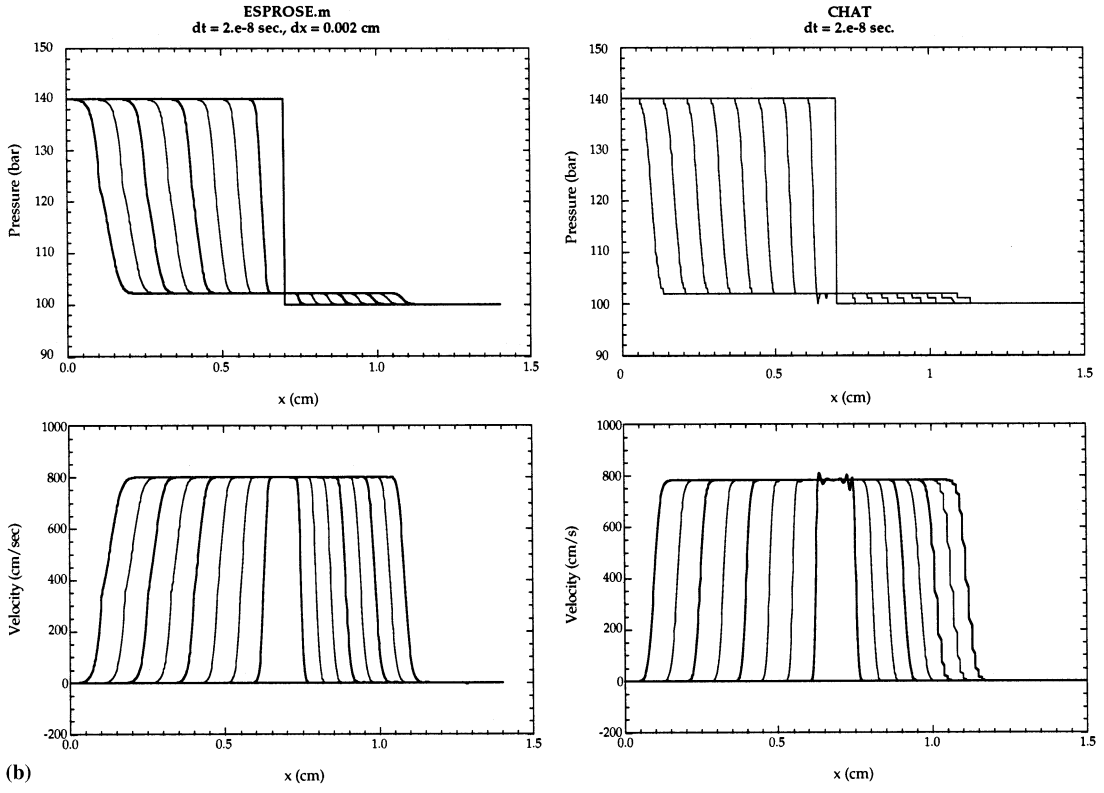

Fig. 7. (b) Comparison between ESPROSE.m and CHAT prediction of the pressure and velocity distributions for the one-dimensional single phase venting problem of (a). (Distributions are plotted at a time interval of 10^{-6} s).

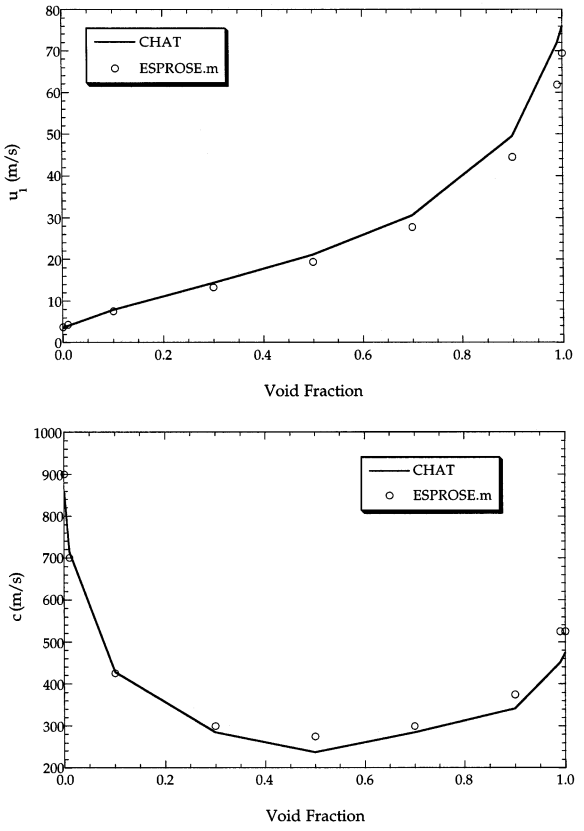

Fig. 8. Comparison between ESPROSE.m and CHAT prediction of the shock speed and fluid velocity for a non-condensible steam/water mixture. (The CHAT solutions are evaluated based on constant-liquid and vapor sound speeds of 600 and 300 m/s respectively. Real properties of water are used in the ESPROSE.m calculation. The incident shock amplitude is 140 bar).

dynamics were obtained, under multiple reflections at the interfaces, for durations up to 6 ms. Representative results are shown together with ESPROSE.m simulations in Fig. 25. We note that while the overall dynamics are captured quantitatively (amplitude and timing of main waves), there is also a secondary structure that is significant, especially in the primary wave. This structure becomes more pronounced as the characteristic void dimension (bubble size) increases, and it may be worth further investigation.

3. Explosion coupling

As a prelude to integral explosions, here we wish to assure that the constitutive laws for microinteractions exhibit, through ESPROSE.m, behaviors consistent with experimental evidence at the elementary level; that is, with detailed observations of single melt drops exploding under simulated large scale explosion condition. Such data were obtained in the SIGMA facility especially for this purpose. The other purpose of this segment of the verification effort was to test the wave dynamics performance of the code near free interfaces in the presence of strong energy sources.

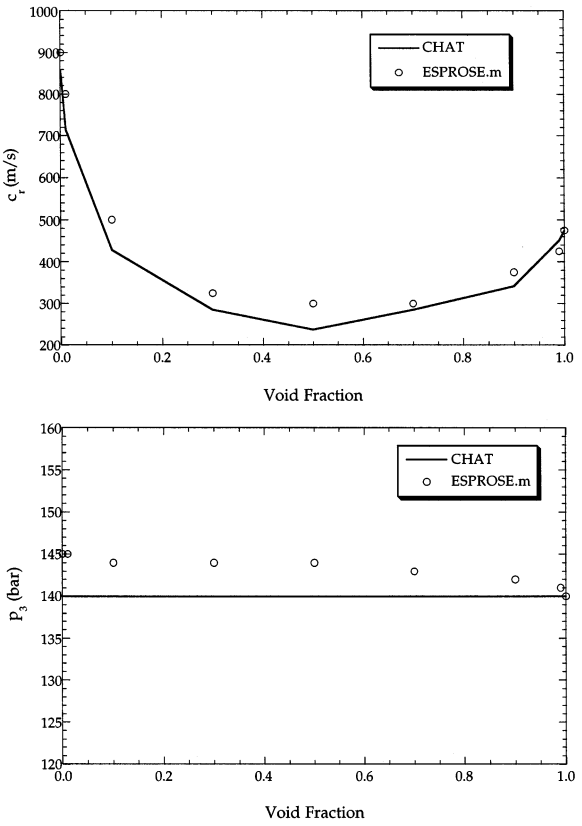

Fig. 9. Comparison between ESPROSE.m and CHAP prediction of the reflected shock speed and shock amplitude for a non-condensible steam/water mixture. (The CHAT solutions are evaluated based on constant liquid and vapor sound speeds of 600 and 300 m/s, respectively. Real properties of water are used in the ESPROSE.m calculation. The incident shock amplitude is at 120 bar).

This was motivated from early tests with the code showing that under strong enough energy sources the pressure venting phenomena (i.e. Section 2.1.2) can be significantly altered. An idealized, but nearly exact numerical model (CHAT) was developed for this purpose, as explained in Appendix B of Theofanous et al. (1995b).

3.1. Analytical tests

3.1.1. Characteristics solutions with explosion coupling

Again, we solve shock tube type problems as in Section 2.1.1. The source terms are selected as

$$Q_l = 0 \qquad Q_g = Cu^{1.5} \tag{11}$$

that is, only the gas phase heated and heating rate increasing with increased fluid motion. This model is chosen to be consistent with the fragmentation physics in ESPROSE.m, which assumes that the energy of the fragmented fuel mass is retained entirely by the 'm-fluid' (gas) phase.

In the first set of calculations (case A), the initial conditions are shown in Fig. 26. The objective was to test the venting of a high pressure wave at a free surface in the presence of an internal heat source. Calculations were carried out for various values of C in Eq. (11), using ESPROSE.m and CHAT. For high values of C, CHAT-QL is used, because the variation of gas density (due to the increase in temperature) becomes important. QL is for quasi-linear, as the equations are still linearized, but gas properties are evaluated at the correct pressure and temperature. To test the effect of a propagating pressure wave venting off a free surface, a second set of calculations (case B) was performed with the initial step pressure starting at a finite distance away from the free surface. The initial conditions are shown in Fig. 27. Comparisons between ESPROSE.m and the characteristics solutions for cases A and B are shown in Figs. 28 and 29, respectively.

In both cases, the comparison shows a remarkable phenomenon that, indeed, a strong enough energy source can 'hang up' the pressure at distances arbitrarily close to a free surface. We have observed the same qualitative behavior in our simulation of steam explosions with a 'calculated' premixture in actual reactor geometry.

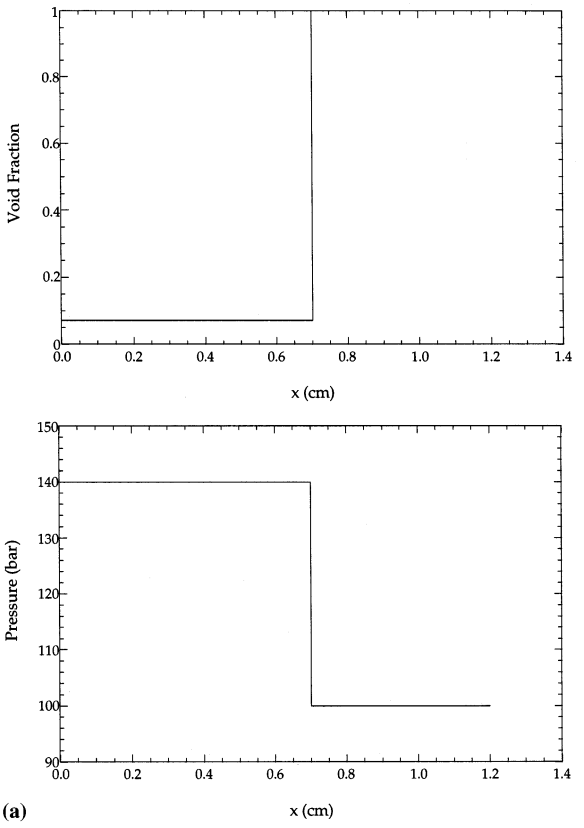

Fig. 10. (a) Initial pressure distribution and void distribution used in the ESPROSE.m/CHAT comparison on pressure venting at a free surface.

Since results in Figs. 28 and 29 were generated with a relatively small grid size (0.002 cm), an additional set of calculations was carried out for case A using grid sizes closer to those used in reactor calculations. The comparison is shown in Fig. 30. The agreement between ESPROSE.m and CHAT/CHAT-QL is good.

3.2. Experimental tests

3.2.1. Constitutive laws for microinteractions

This segment of the work is not so much verification, as it is making sure that the fundamental component of an explosion, the microinteractions,

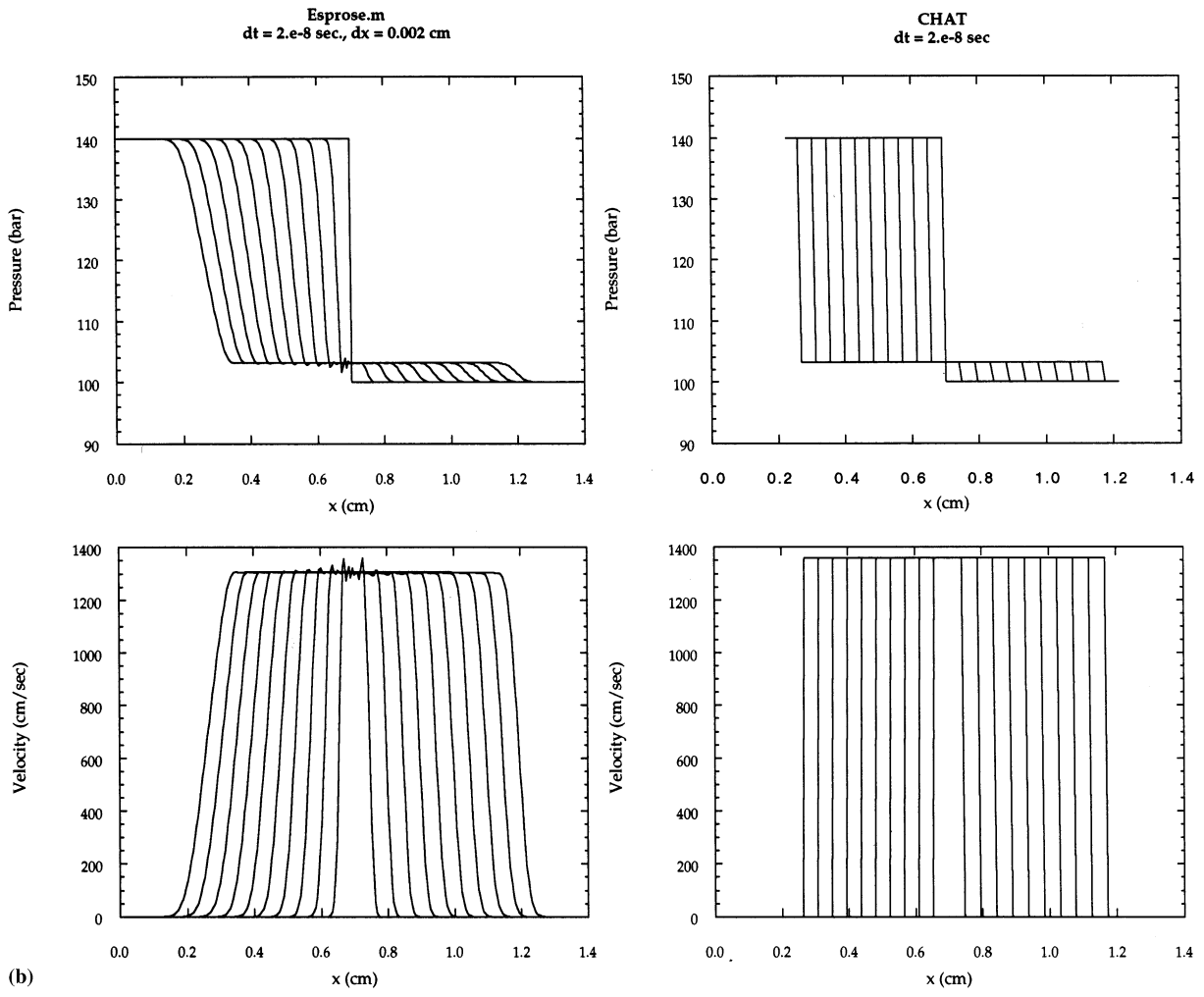

Fig. 10. (b) Comparison between the ESPROSE.m and CHAT prediction of the pressure and velocity distributions for the one-dimensional two-phase venting problems of (a). (Distributions are plotted at a time interval of 10^{-6} s).

is properly represented in, and captured by, the code. The basis is provided by experiments in the SIGMA facility. The code simulations of these experiments are used to extract the descriptions of fragmentation rate and quantities of coolant involved in the microinteractions, in terms of local, instant processes, as described in Chen et al., (1995). This work included mostly tin melts. More recent results for iron melts and temperatures up to 2000 K can be found in Chen et al., 1997. Work is currently continuing for ZrO_2 melts and temperatures up to ~ 3000 K.

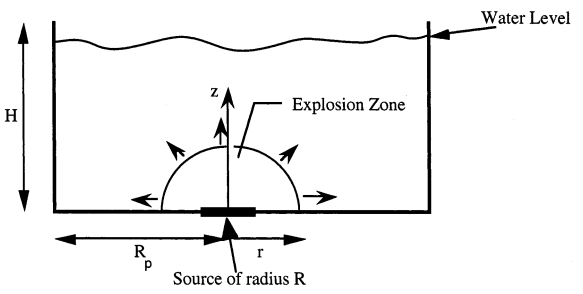

Fig. 11. The geometry for an axisymmetric, open pool, explosion.

Table 3
Summary of test cases for 2D wave dynamics

	Geometry		
Source type	Infinite pool $0<r<\infty$	Cylindrical open pool $0<z<H$, $0<r<R_p$	Cylindrical closed pool $0<z<H$, $0<r<R_p$
(A)[a] $n=1$	Eq. (9)[a] (Figs. 14 and 16)	Superposition (Figs. 14 and 16)	Superposition (Figs. 14 and 16)
(B)[a] $n=1$	Eq. (9)[a] and Eq. (10)[a] (Figs. 15 and 17)	Superposition (Figs. 15 and 17)	Superposition (Figs. 15 and 17)

[a] See Table 4

4. Integral aspects

In this section, we put together wave dynamics and microinteractions to determine whether steam explosions can be predicted on a consistent basis; that is, with realistic fuel and void concentrations, and fragmentation rates. At the foundation of this task are the KROTOS experiments. The data include triggered and spontaneous propagations in a 1D geometry, with tin, aluminum oxide, and uranium oxide melts, with widely different behaviors. At the other end of this effort are some analytical tests, including comparisons of ESPROSE.m against the newly developed ESPROSE.m 3D. Finally, as another benchmark, we compare ESPROSE.m against exact solutions obtained for steady-state detonations with microinteractions (Appendix D of Theofanous et al. (1995b), and Yuen and Theofanous (1997)). The presentation below is in the reverse order.

4.1. Analytical tests

4.1.1. Exact solutions for steady detonations

The extension of the now classic steady-state detonation theory of Board and Hall to the 'microinteractions' concept is presented in Appendix D of Theofanous et al. (1995b). Here, we push ESPROSE.m to extremely high fragmentation rates and examine the results in relation to the

Table 4
Elementary solutions used in superposition computations[a]

Source type A: $u_r(R,t)=A_n t^n$

$$\frac{p-p_\infty}{\rho c A_n}=\frac{R}{r}\left\{\sum_{j=0}^{n-1}(-1)^j\frac{n!\left[t-\dfrac{r-R}{c}\right]^{n-j-1}}{(n-j-1)!\left(\dfrac{c}{R}\right)^{j+1}}+\frac{(-1)^n n!}{\left(\dfrac{c}{R}\right)^n}\exp\left[-\frac{ct}{R}+\frac{r}{R}-1\right]\right\} \tag{9}$$

Source type B: for $t<t_0$ $u_r(R,t)=A_n t^n$, for $t>t_0$ $u_r(R,t)=A_n t_0^n$

$$t<t_0\quad \frac{p-p_\infty}{\rho c A_n}=\frac{R}{r}\left\{\sum_{j=0}^{n-1}(-1)^j\frac{n!\left[t-\dfrac{r-R}{c}\right]^{n-j-1}}{(n-j-1)!\left(\dfrac{c}{R}\right)^{j+1}}+\frac{(-1)^n n!}{\left(\dfrac{c}{R}\right)^n}\exp\left[-\frac{ct}{R}+\frac{r}{R}-1\right]\right\}$$

$$t>t_0 \text{ and } \frac{r}{R}<1+\frac{c(t-t_0)}{R}$$

$$\frac{p-p_0}{\rho c A_n\left(\dfrac{R}{c}\right)^n}=\frac{R}{r}\left\{\sum_{j=0}^{n-1}\frac{(-1)^j n!\left[\dfrac{c}{R}t-\dfrac{r}{R}+1\right]^{n-j-1}}{(n-j-1)!}+\exp\left\{-\frac{c}{R}(t-t_0)+\frac{r}{R}-1\right\}\sum_{j=1}^{n}\frac{(-1)^j\left(\dfrac{ct_0}{R}\right)^{n-j}}{(n-j)!}\right\} \tag{10}$$

$$t>t_0 \text{ and } \frac{r}{R}=1+\frac{c(t-t_0)}{R}\quad p-p_0=0$$

[a] A_n, source constant; $A_n<0$ sink, $A_n>0$ source; p_∞, pressure at infinity, initial pressure; ρ, liquid density; c, velocity of sound in liquid; R, source radius; R_p, pool radius; t, time; and p_0, pressure at time t_0.

Hugoniot and Rayleigh lines of detonation theory.

As an example, consider a uniform premixture with 5% tin at 1500°C and 5% void, in a 1D geometry. For purposes of illustration, we assume a coolant entrainment factor of $f_e = 1$ (for definition of f_e, see Chen et al., 1997). The calculation is carried out with a 'fast' constant fragmentation rate of 10^5 g s^{-1} cm^{-3}. The development of the transient pressure and velocity distribution of the detonation are shown in Figs. 31 and 32. To gain a perspective of the numerical solution relative to the steady state analytical solution, the 'developed (ESPROSE.m)' pressure distribution (taken at 70

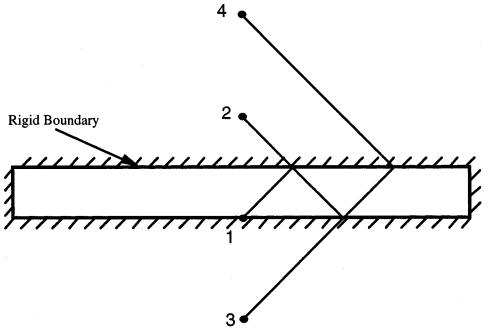

Fig. 12. Illustration of the superposition process for a closed cylindrical pool. The solid circles indicate sources of equal strength. The number shows the order of incorporation, but the time origin in the elementary solutions superposed is always the same.

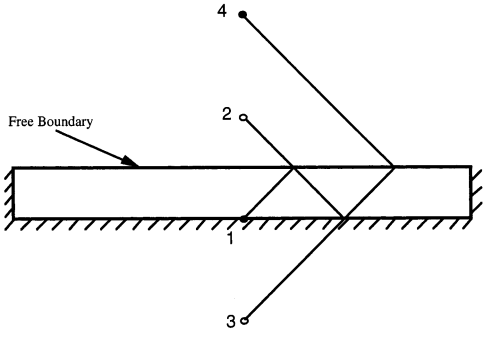

Fig. 13. Illustration of the superposition process for an opened cylindrical pool. The solid circles indicate sources of equal strength while the open circles indicate sinks of equal strength. The number shows the order of incorporation, but the time origin in the elementary solutions superposed is always the same.

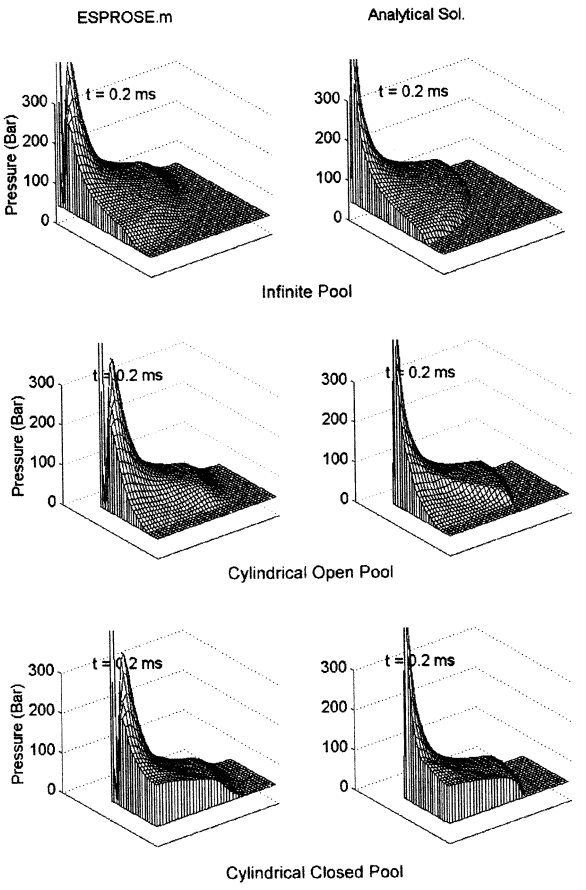

Fig. 14. Comparison between ESPROSE.m and the analytical prediction of the two-dimensional pressure distributions at $t = 0.2$ ms with source type A. (The mass source parameters are $A_1 = 10^9$, $n = 1$ and $R = 1.414$ cm. ESPROSE.m data are generated with $\Delta r = \Delta z = 1$ cm and $\Delta t = 10^{-6}$ s.)

μs) is plotted in p–v coordinates along with the shock adiabat and the Hugoniot in Fig. 33. In Fig. 33, we can locate the tangent Rayleigh line which determines the von Neumann spike and the C–J point at ~3000 and 1300 bar, respectively.

The determination of the C–J point and the physical behavior of the detonation wave is further illustrated by Fig. 34. In this figure u_1 is the velocity of the shock relative to the premixture which is at rest. The tangency condition is equivalent to a minimum in u_1 and as shown in Fig. 34, this leads to a C–J pressure of 1300 bar. The tangency condition can also be interpreted (Landau and Lifshitz, 1959) as a state at which

the detonated mixture velocity relative to the shock front (u_2) equals its sound speed (i.e. the detonated mixture is sonic). This choking condition leads to a C–J pressure of 1200 bar. This discrepancy between the two predictions can be attributed to the broad minimum of u_1 and the propagation of numerical error in determining its value. Finally, the wave speed of the detonation wave (the speed of constant pressure points on the pressure profiles in Fig. 31) is also plotted in Fig. 34. We can see that the wave becomes sonic exactly at the C–J point, and remain sonic in the expansion region behind it. This expansion section is self-similar as the pressure wave 'fans out' with the reduction of speeds along the Hugoniot. Ahead of the C–J point, the speed of the shock front is slightly higher and settles to a steady value which is locally subsonic.

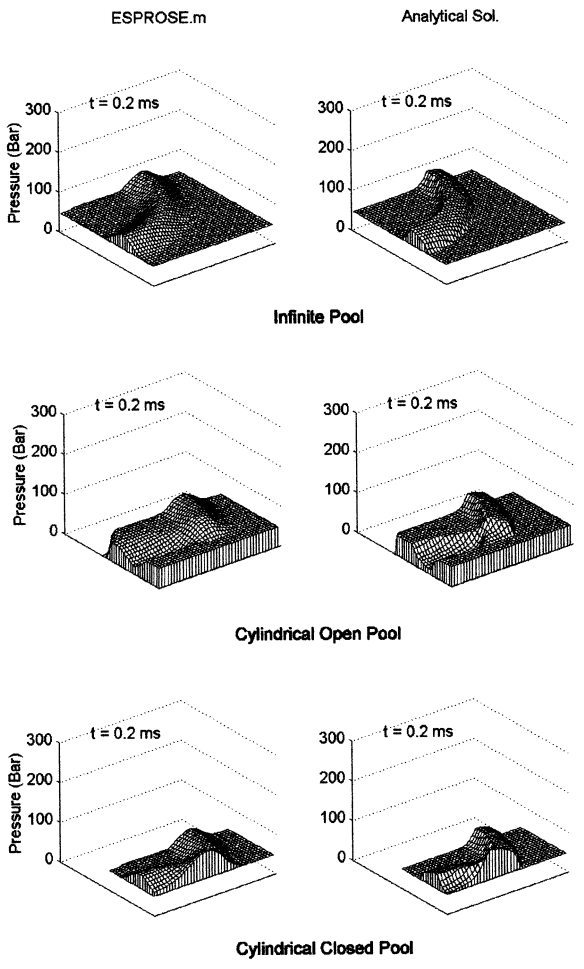

Fig. 15. Comparison between ESPROSE.m and the analytical prediction of the two-dimensional pressure distribution in an infinite pool with source type B. (The mass source parameters are $A_1 = 10^9$, $n = 1$ and $R = 1.414$ cm and $t_0 = 5.e-5$ s. ESPROSE.m data are generated with $\Delta r = \Delta z = 1$ cm and $\Delta t = 10^{-6}$ s.)

4.1.2. Effect of rate processes on exact solutions

Now, the numerical results of the previous section are examined in relation to additional calculations carried out with the fragmentation/microinteraction laws in ESPROSE.m. First, relaxing just the fragmentation rate, we obtain the results shown in Fig. 35. Second, relaxing also the entrainment factor to the value normally used in ESPROSE.m, we obtain the results shown in Fig. 36. Note that with each successive approach to realistic conditions we depart from the strong detonation of Figs. 31 and 32, to a relatively slowly evolving propagation without the main shock, to a very mild event that could hardly be characterized as energetic. This is in agreement with the KROTOS test results. In Section 4.2, we show that the ESPROSE.m treatment can capture also the strong detonations observed in KROTOS with aluminum oxide melts.

4.1.3. ESPROSE.m to ESPROSE.m-3D comparisons

One purpose of these comparisons was to verify the equivalence between the newly developed ESPROSE.m-3D and the extensively tested ESPROSE.m. The other purpose to a mutual benefit was to demonstrate the robustness of the two, quite different, numerical schemes for this class of problems.

Explosion calculations were carried out with both codes in 1D and 2D geometries. First, for the 1D, ESPROSE.m results were compared to 1D results obtained with the 3D code run in each of the three coordinate directions (x, y, and z). The comparisons were excellent. Second, ESPROSE.m-3D was applied to an axisymmetric (cylindrical) geometry, and compared with ESPROSE.m. The case was an ex-vessel explosion in a large (9 m diameter, 3 m deep) pool. The 3D

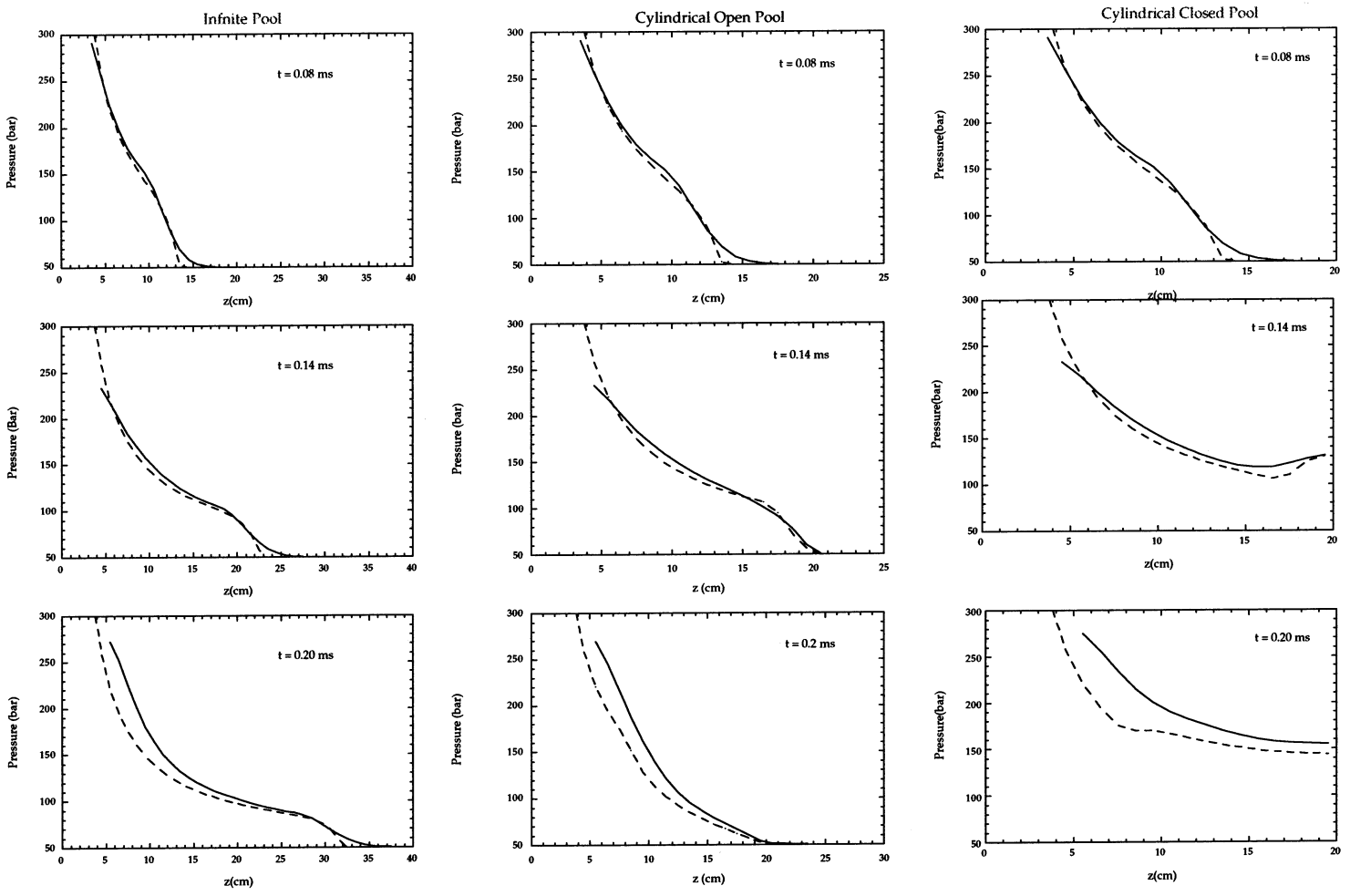

Fig. 16. Comparison between ESPROSE.m and the analytical solution for the centerline pressure distribution ($r = 0$) at three different times for the three cases with source type A. (All parameters are identical to those specified in Fig. 14.)

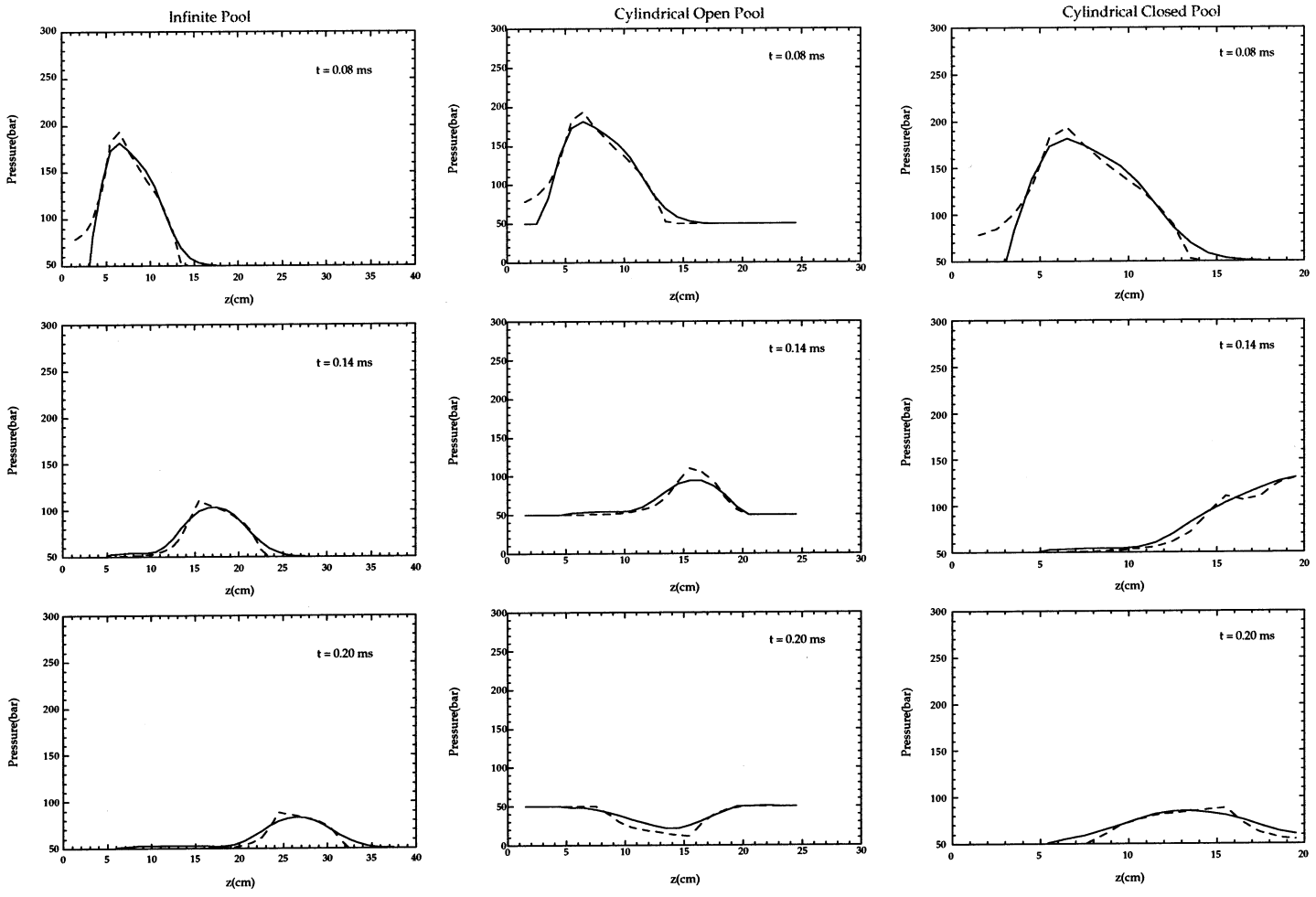

Fig. 17. Comparison between ESPROSE.m and the analytical solution for the centerline pressure distribution ($r = 0$) at three different times for the three cases with source type B. (All parameters are identical to those specified in Fig. 15.)

code produced a very nearly axisymmetric result. The peak pressures, anywhere in the explosion zone, and typical pressure transients at the wall, are compared in Figs. 37 and 38, respectively. For the 3D code, a check of axisymmetry is shown in Fig. 39.

4.2. Experimental tests

4.2.1. Comparisons with KROTOS experiments

There have been, so far, three kinds of qualitatively different results from these experiments: weak propagation with tin at ~ 1000 K, strong supercritical explosions with aluminum oxide at ~ 2700 K, and no propagation with uranium dioxide at ~ 3000 K. The uranium oxide results were attributed to extensive voiding at the test section (Huhtiniemi et al., 1995). The explosion results can be further divided into two groups depending on the initial water subcooling. For tests with low subcooling (about 10 K or less), an external trigger is needed to start the explosion. For tests with high subcooling (about 80 K), the mixture explodes spontaneously prior to fuel reaching the bottom of the test section. The ESPROSE.m's interpretation of the explosion behavior of two tests with external trigger (KROTOS-21 with tin and KROTOS-27) can be found in Theofanous et al. (1995b). The current effort will focus on the more recent test with spontaneous explosions (KROTOS-38) and one uranium oxide test (KROTOS-45).

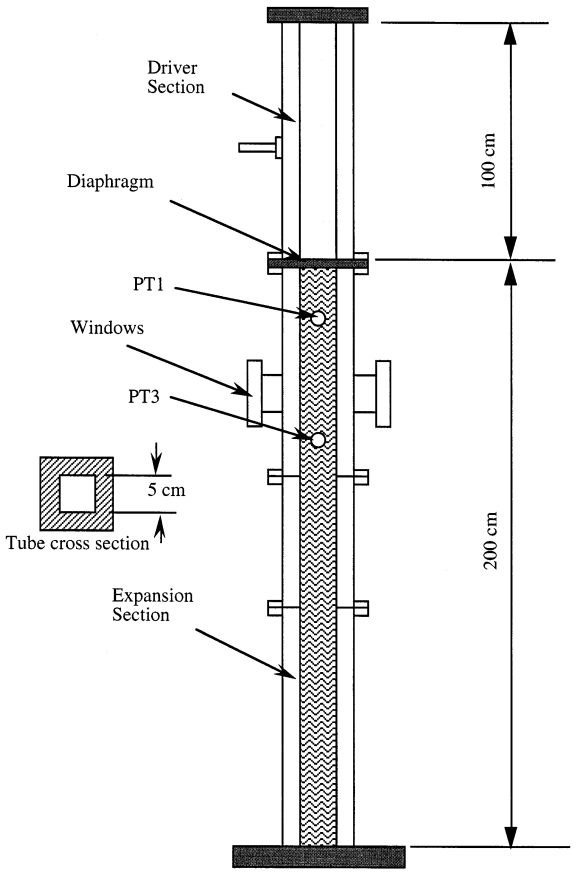

Fig. 18. Schematic of the SIGMA shock tube.

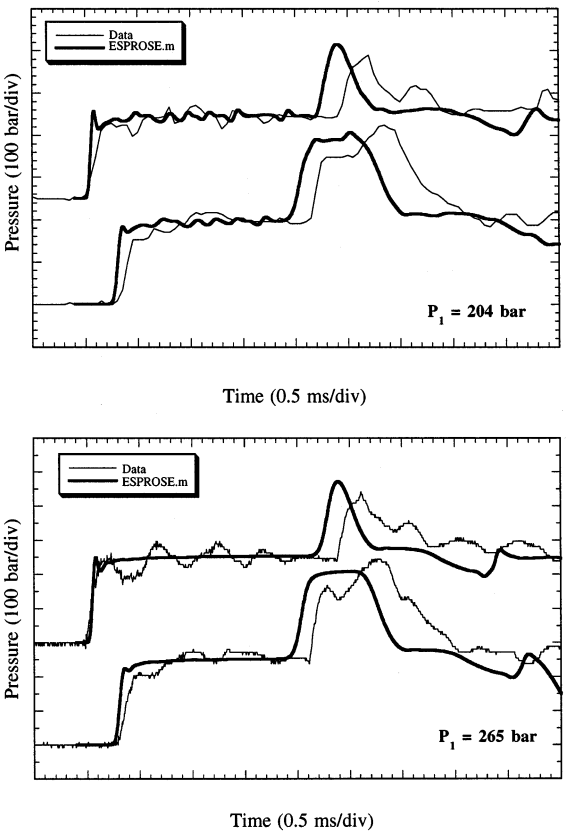

Fig. 19. ESPROSE.m simulation of pressure transducers PT1 and PT3 for two SIGMA runs with all liquid in the expansion section. Whole time scale is 5 ms.

For KROTOS-38, we use PM-ALPHA.L-2D and ESPROSE.m-2D for the premixing and explosion analysis. The discretization is shown in Fig. 40. A gravity-driven melt delivery model is developed to simulate the fuel inlet. The delivery opening was 3 cm. The initial length scale of the fuel is taken to be 1 cm and further breakup is assumed to be negligible.

The advancement of the melt penetration front is shown in Fig. 41. The thermocouples exhibit a clearly erratic behavior, but this is not unexpected, since with such a high subcooling they must be subject to direct 'hits' in order to feel the melt. Given the rather low area-averaged melt volume fraction, it is not at all surprising to have some delayed hits. This is clearly the case for the first thermocouple, so it is shown as an open circle. The remaining show a clear trend, if we also exclude the fourth thermocouple, again assuming a delayed hit. This is also shown as an open circle. That this is the proper trend is also supported by the independent determination of the two extremes (they make the two very reliable anchors in the data). One is the near surface thermocouple ($z = \sim 100$ cm), where the melt arrives under free-fall. The other is at a position around the K3 transducer ($z = \sim 55$ cm), where the explosion appears to have been triggered (spontaneously) at ~ 1 s. Further, it should be

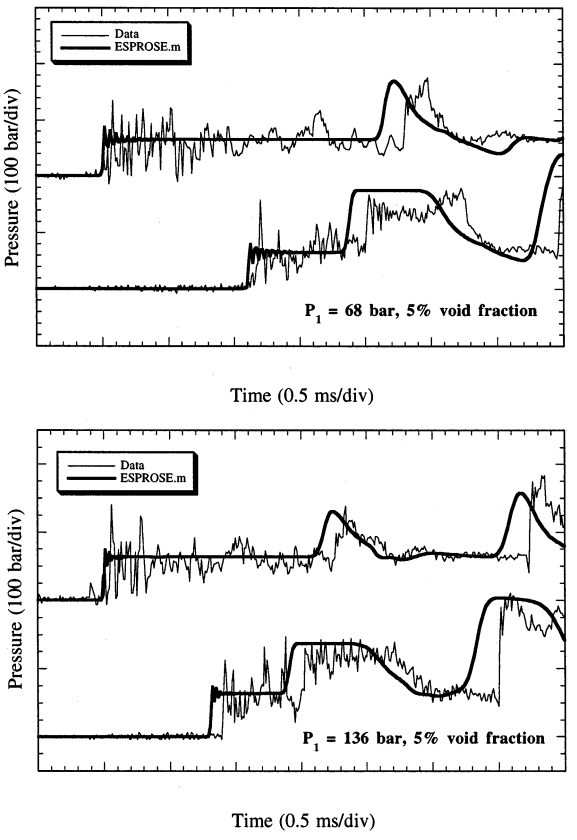

Fig. 20. ESPROSE.m simulation of pressure transducers PT1 and PT3 for two SIGMA runs with a liquid/air mixture in the expansion section. Whole time scale is 5 ms.

Table 5
Experimental conditions, results, and comparisons with predictions for all two-phase (air–liquid) SIGMA runs

Run ID	Pressure (bar)	Void fraction (%)	Bubble diameter (mm)	Shock speed (m/s)		
				Experimental	ESPROSE.m	Analytical
PPB	204	10	30	285	500	475
Bubble I	68	10	7	296	285	275
Bubble II	68	30	24	147	160	180
Bubble III	136	30	24	190	222	250
Bubble IV	68	10	25	258	285	275
Bubble V	68	5	18	357	363	378
Bubble VI	68	5	25	320	363	378
Bubble VII	68	7.8	7	307	280	307
Bubble VIII	136	5	7	533	507	535
Bubble IX	136	5	18	444	507	535
Bubble X	68	3.5	7	412	426	448
Bubble XI	68	2.5	7	500	496	528

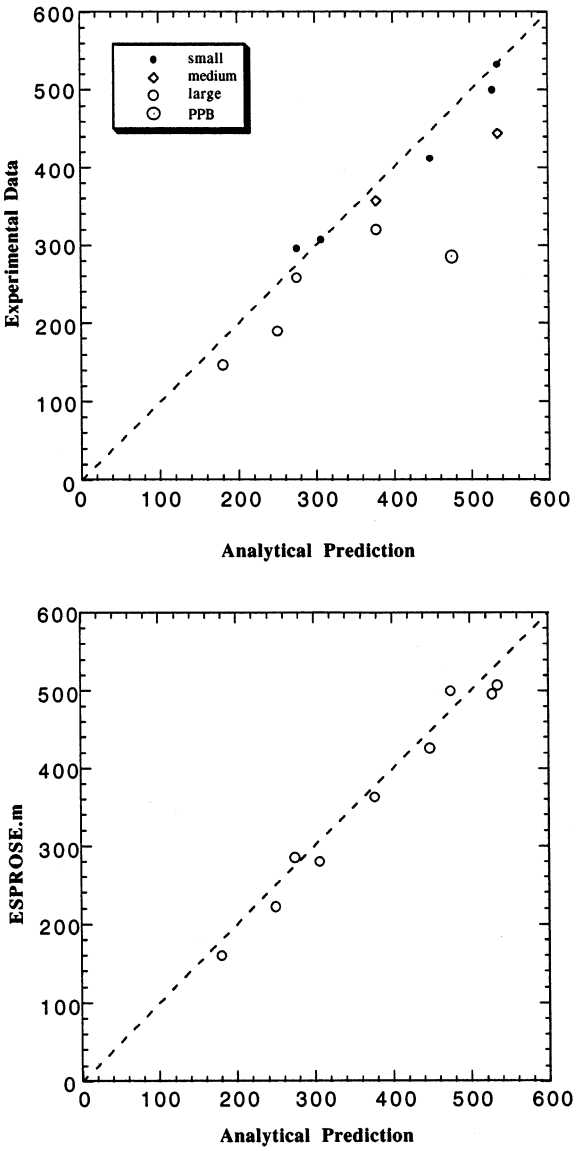

Fig. 21. Comparison between predicted (both analytically and by ESPROSE.m) and experimental (SIGMA) shock speeds (m/s) for all two-phase runs.

noted that this aspect of the computation is rather reliable, because it is not complicated by significant phase change effects (the average void fraction surrounding the fuel at the time of the explosion was only 5%).

Selected frames to visualize the PM-ALPHA.L-2D results are collected in Fig. 42. Again, for

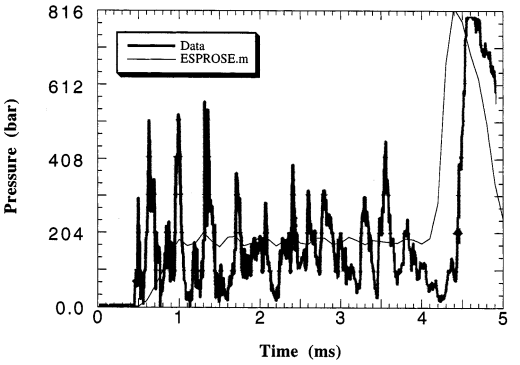

Fig. 22. Individual collapse events in the PPB run, reflected wave measured, and the ESPROSE.m prediction. $p_1 = 204$ bar.

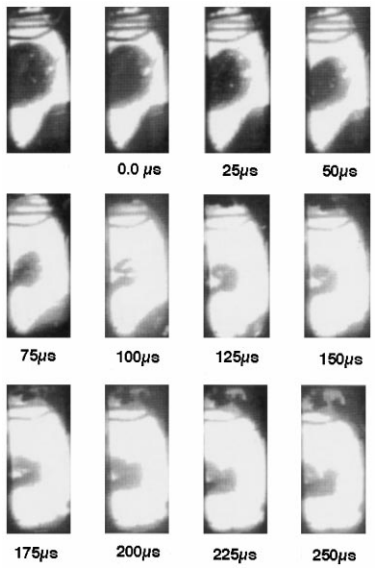

Fig. 23. The collapse of an air 'bubble' in run bubble IX.

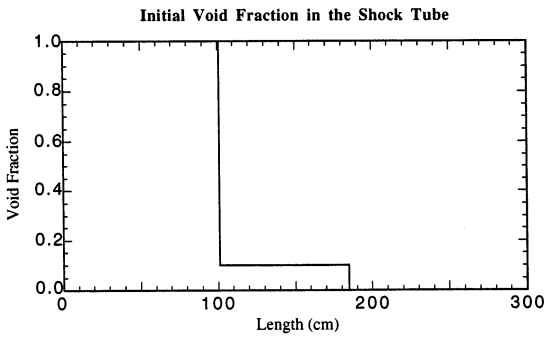

Fig. 24. The axial void fraction distribution used in the multiregion SIGMA runs.

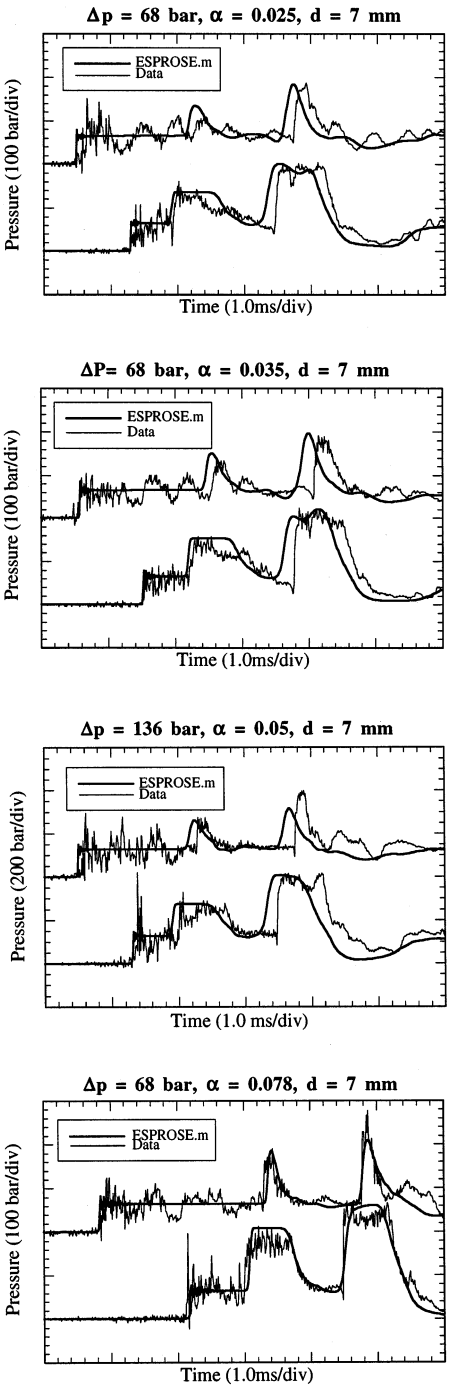

Fig. 25. ESPROSE.m simulation of the multiregion SIGMA runs. Whole pressure and time scales are 600 bar and 6 ms, respectively.

clarity, each particle shown represents a 'cluster' of particles. We can see that due to the high subcooling, short times, and relatively low melt plunging velocity (absence of strong breakup), the premixing proceeds rather quietly, with imperceptible void formation. More specific quantitative representations of these results are shown in Figs. 43 and 44. In particular, in Fig. 44, we see that the melt remains mostly confined in the core region, where it reaches local volume fractions of 30%. In Fig. 43, we see that the void fraction remains at nearly zero, except in regions surrounding the fuel where it reaches an average value of 5%.

The premixing result at 1 s was triggered in ESPROSE.m-2D, by releasing the pressure from the innermost computational cell at the elevation of K3 (55 cm), assumed to be saturated at a pressure of 100 bar. Calculations were carried out with the microinteractions parameters as deter-

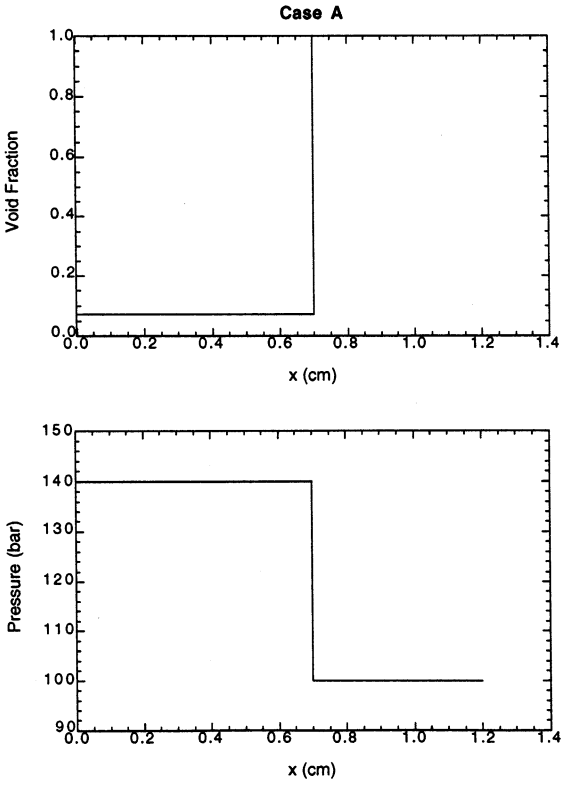

Fig. 26. Initial void fraction and pressure distribution for test case A.

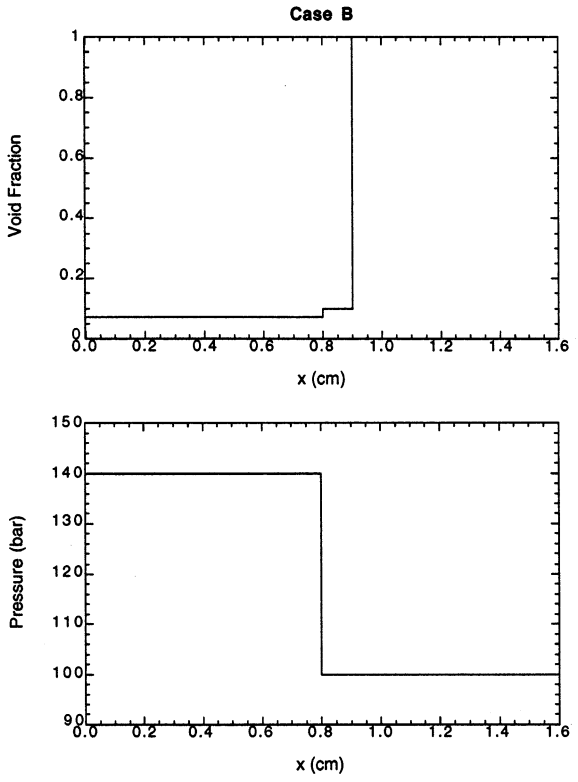

Fig. 27. Initial void fraction and pressure distribution for test case B.

mined from the SIGMA experiments ($\beta_f = 9$, $f_e = 7$). Results are presented in Fig. 45 and they are in excellent agreement with experiments. It is interesting to note that although there is no melt in the lower $\sim 1/2$ of the tube the impulse obtained therein is significantly larger than the upper region. The dynamics here involve the explosion propagating upwards (K3 → K4 → K5), while at the same time pressures try to vent downward (K3 → K2 → K1 → K0). Not containing any significant compressible volume, this lower part pressurizes, and even more so as this pressure wave reflects from the bottom, rigid, surface.

In KROTOS-45, excessive voiding led to pressurization of the test section. To simulate this behavior, it is necessary to account for the freebound volume (0.1 m^3) which is significantly larger than the volume of the initial water column (0.03 m^3). PM-ALPHA.L-3D, which can be readily extended to have a finite number of 'freeboard volume' cells with large grid size, is used to simulate the premixing process.

Using a test section grid size of $\Delta x = \Delta y = \Delta z = 4.4$ cm, the melt front propagation and test section pressurization are simulated well with an initial melt length scale of 0.5 cm and a breakup parameter, β, of ~ 30. Results are presented in Figs. 46 and 47. The rapid initial pressure rise at the initial fuel penetration into the water (at 0.25 s) is probably due to an initial rapid breakup of the fuel. While this trend can be captured by a more detailed modeling of the breakup parameter, it is beyond the scope of the current verification effort. The premixing maps (Fig. 48) for the case with $\beta = 30$ indicate rather extensively voided premixtures early in the transient. Past 0.7 s, the voiding subsides as subcooling builds up with pressure quite rapidly, but by that time most melt particles are already frozen by more than 50%. In this premixing history there is no opportunity for triggering, which is consistent with experimental findings.

5. Numerical aspects

5.1. Space/time discretization

With available computing power for in-vessel explosions, we can go down to centimeter-scale nodes, even for 3D representations. Thus, at this time, representation (accuracy) issues due to discretization, at present, arise only for very large ex-vessel geometries. This limitation will be overcome in the near future by implementing adaptive gridding to allow for fine nodes in the explosion zone, and large nodes in the surrounding water, where one needs only to capture the relatively simple wave dynamics. With respect to time discretization, we have found the proper domains to obtain robust and accurate computations, and this has not been a problem.

5.2. Numerical diffusion

Numerical diffusion is always present; however, with the guidance provided from the various

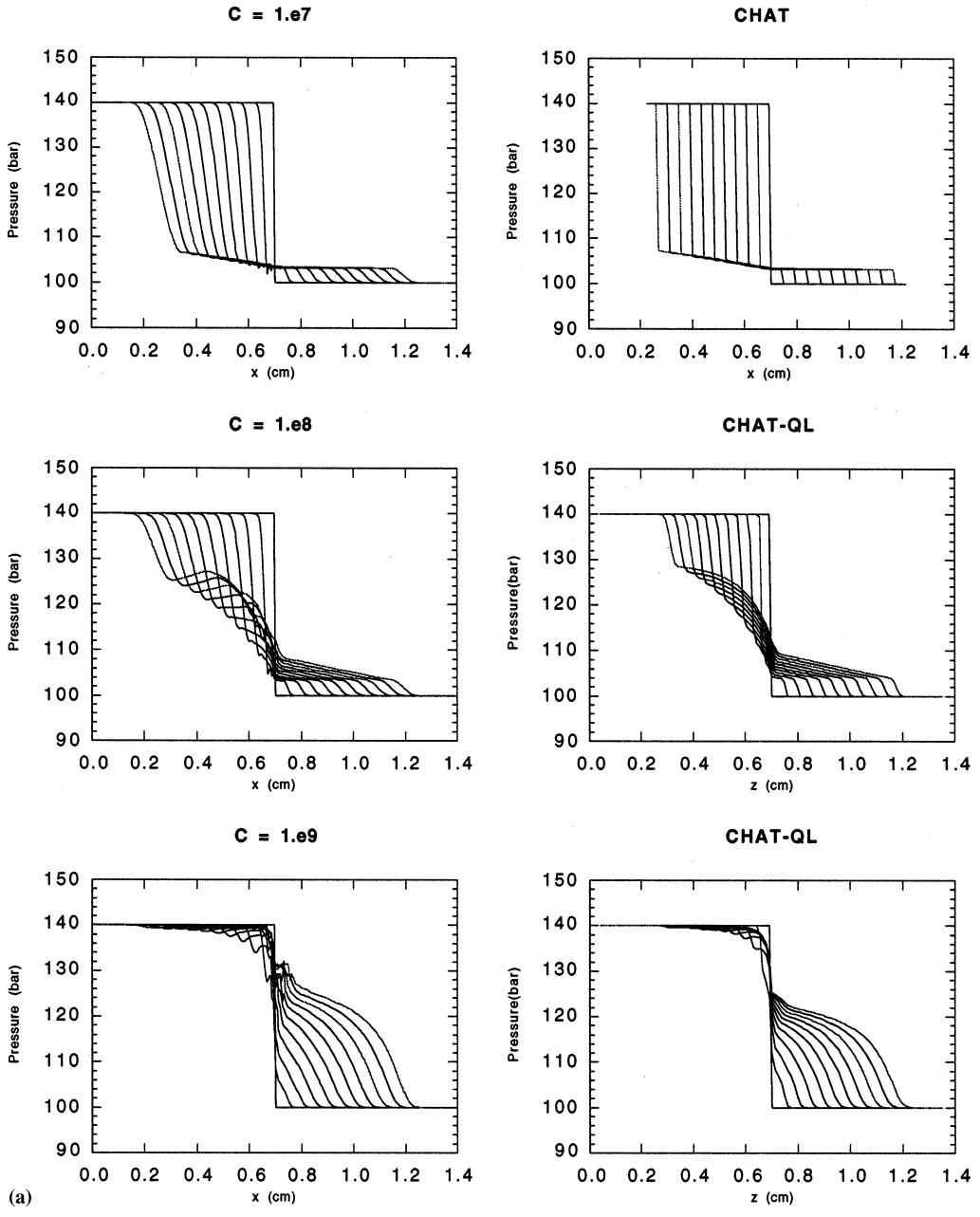

Fig. 28. (a) Pressure distributions predicted by ESPROSE.m and those generated by CHAT/CHATQL for test case A. Profiles are plotted in intervals of 10^{-6} s. The ESPROSE.m calculations use a grid size of $dx = 5 \cdot 10^{-3}$ cm and a time step of $2 \cdot 10^{-8}$ s. The CHAT/CHAT-QL solutions are generated with a time step of $2 \cdot 10^{-3}$ s.

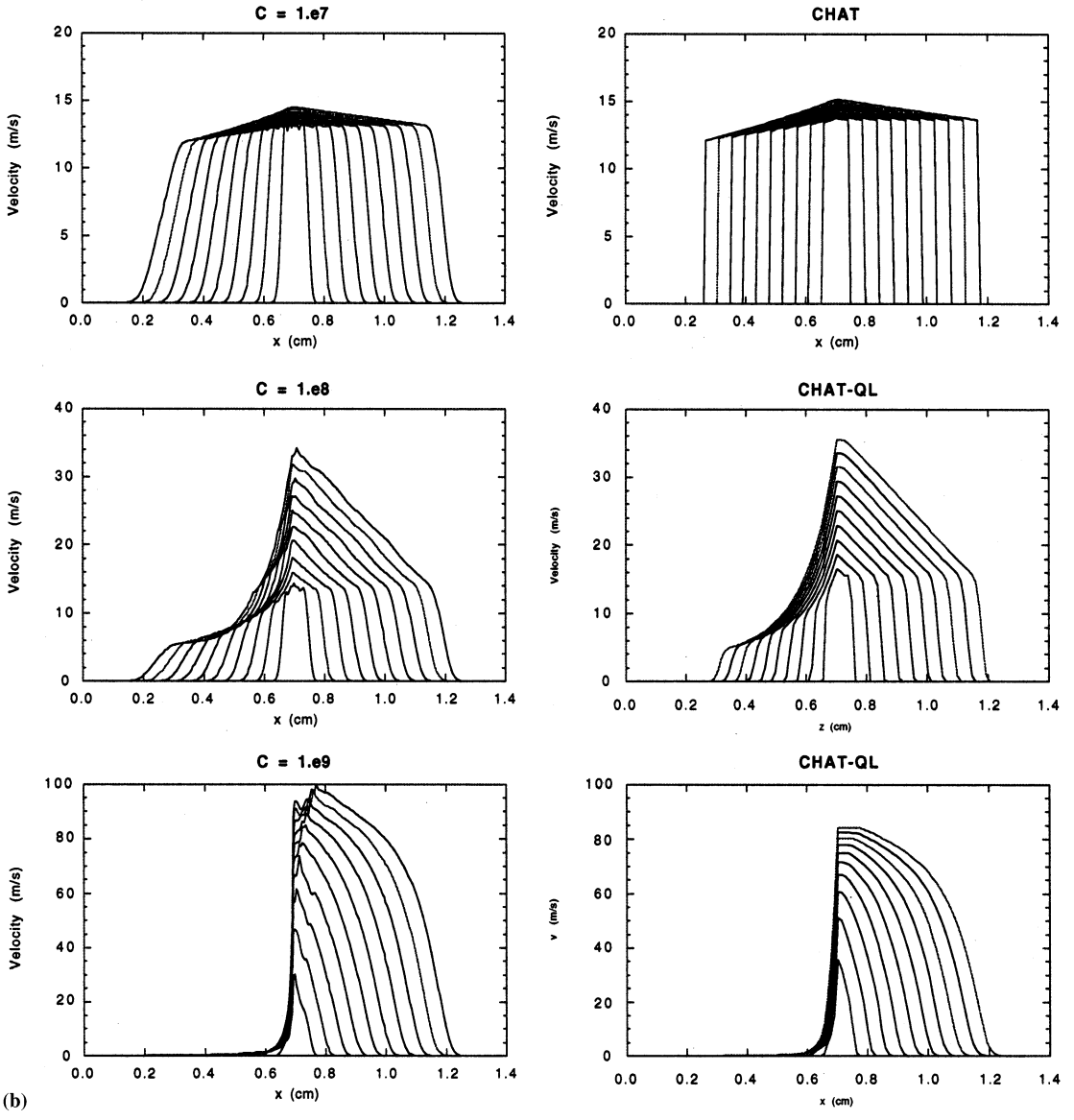

(b)

Fig. 28. (b). Velocity distributions predicted by ESPROSE.m and those generated by CHAT/CHAT-QL for test case A. (Numerical parameters are identical to those of (a).)

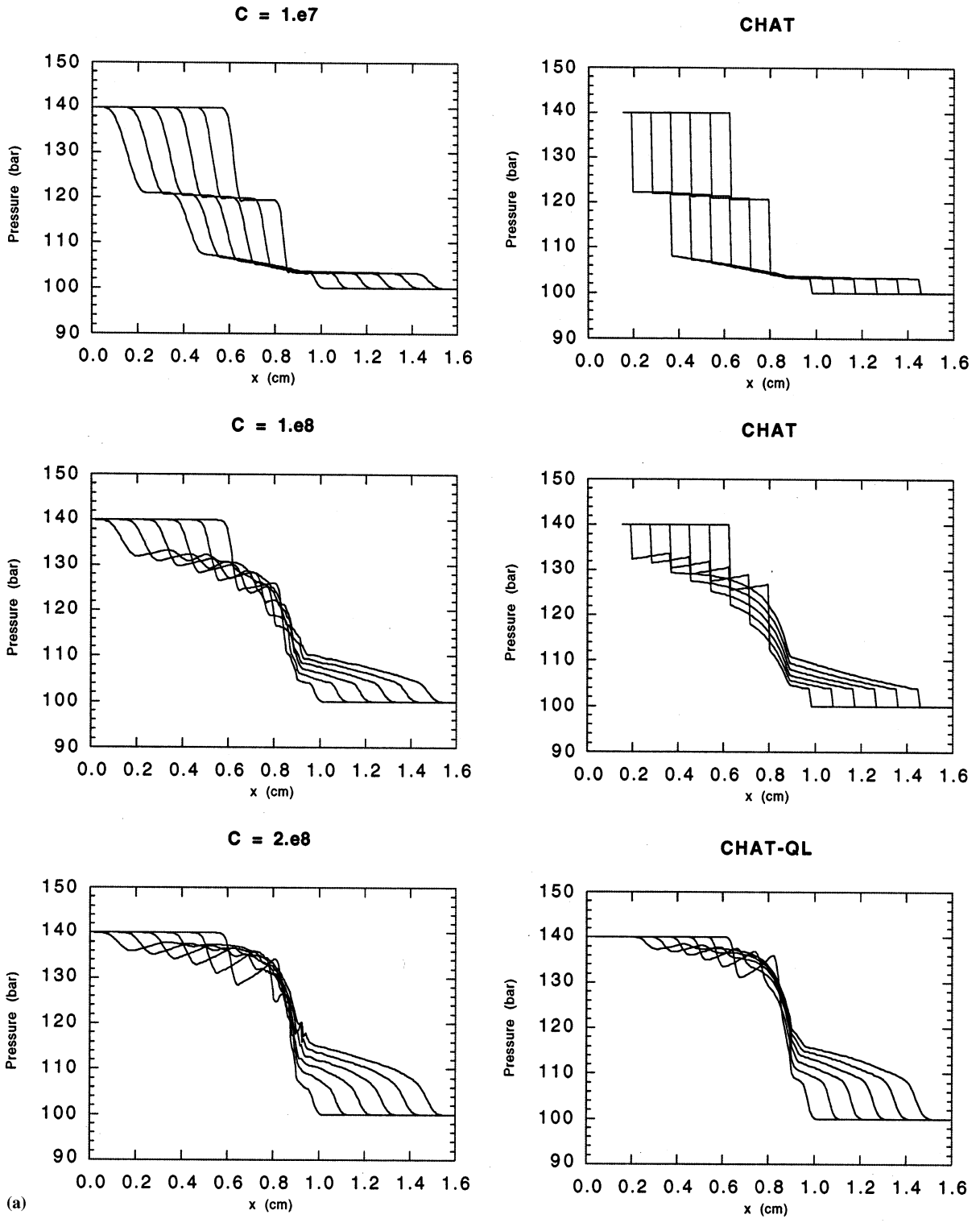

Fig. 29. (a). Pressure distributions predicted by ESPROSE.m and those generated by CHAT/CHAT-QL for test case B. Profiles are plotted in intervals of 10^{-6} s. The ESPROSE.m calculations use a grid size of $dx = 5 \cdot 10^{-3}$ cm and a time step of $2 \cdot 10^{-8}$ s. The CHAT/CHAT-QL solutions are generated with a time step of $2 \cdot 10^{-3}$ s.

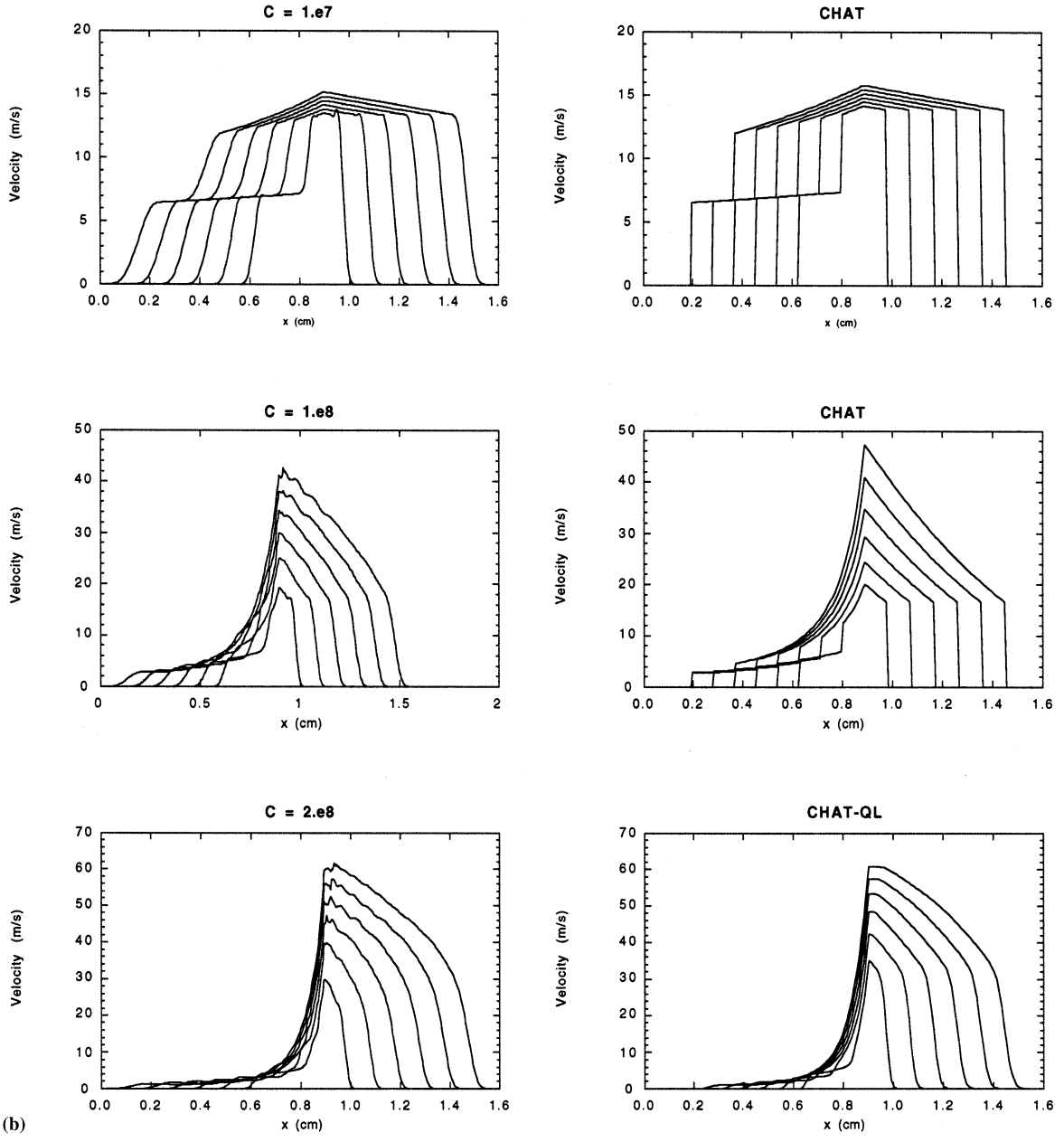

(b)

Fig. 29. (b) Velocity distributions predicted by ESPROSE.m and those generated by CHAT/CHAT-QL for test case B. (Numerical parameters are identical to those of (a).)

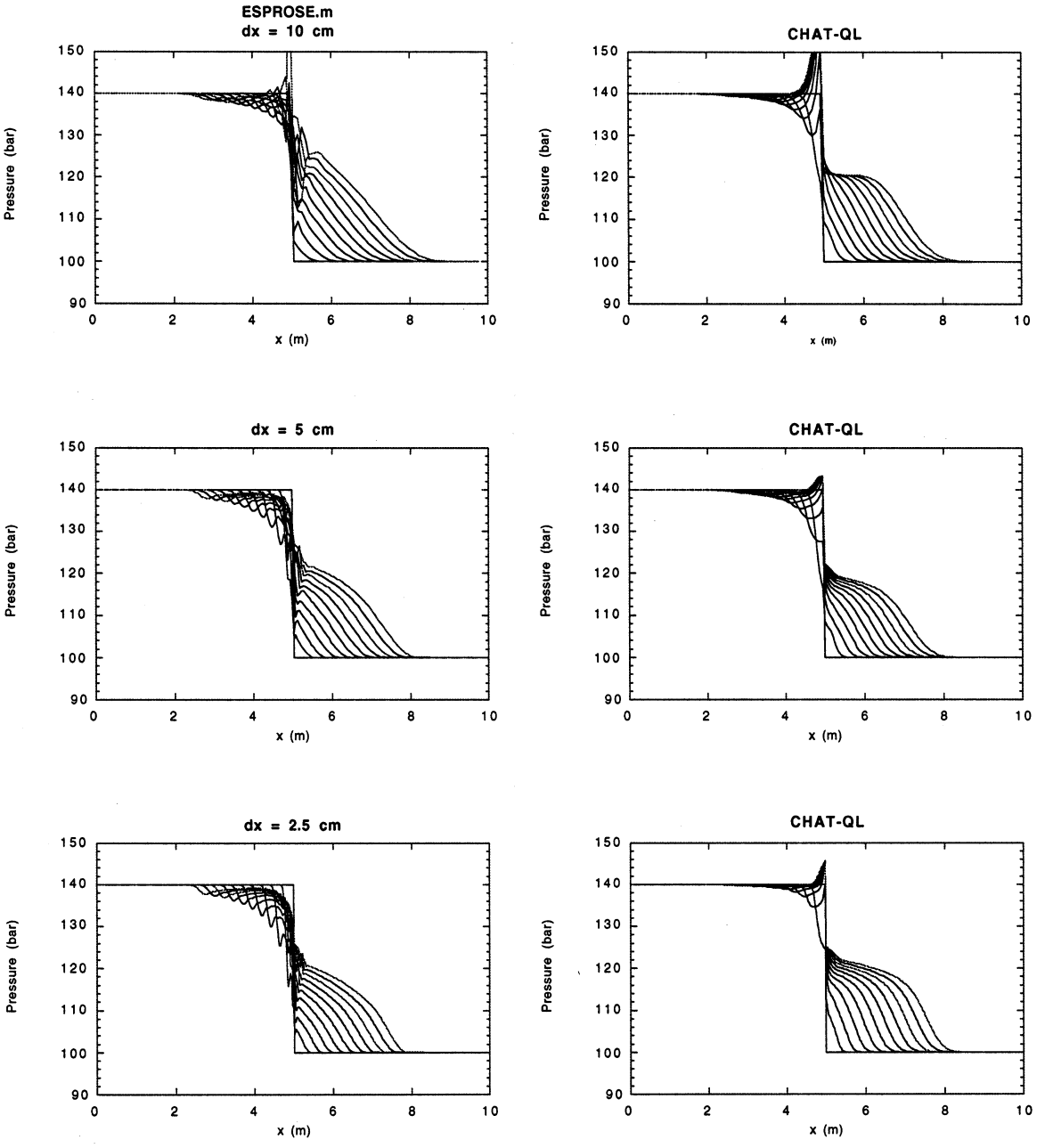

Fig. 30. Comparison between ESPROSE.m results for different grid sizes and those generated by CHAT-QL. (The initial conditions are those of case A with $C = 10^6$. Profiles are plotted at intervals of $5 \cdot 10^{-4}$ s.)

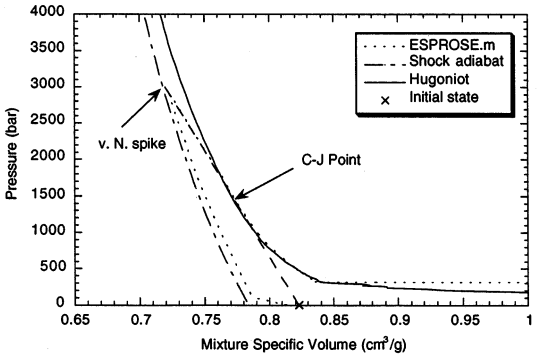

Fig. 31. Illustration of escalation and approach to steady state in an ESPROSE.m simulation of a tin-water explosion, with a premixture void fraction of 5% and fuel fraction of 5%. Print interval is 5 μs.

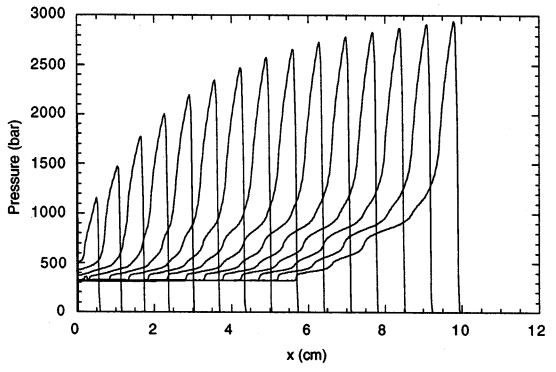

Fig. 32. Mixture velocity corresponded to the pressure distribution shown in Fig. 31.

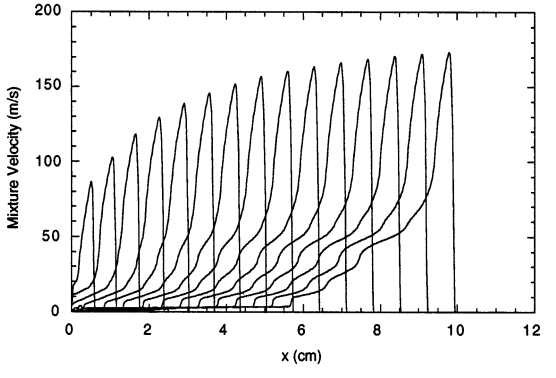

Fig. 33. The ESPROSE.m result at 70 μs in the p–v plane, in relation to the shock adiabat, the Hugoniot, the C–J point and the von Neumann spike.

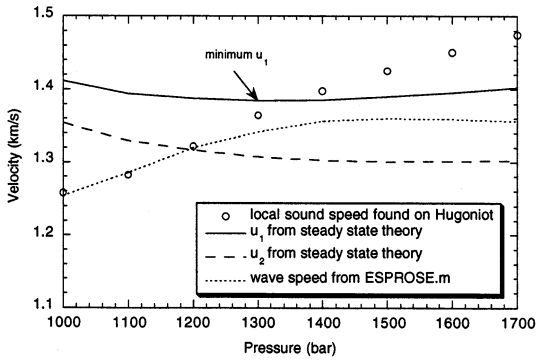

Fig. 34. Demonstration of choking at the C–J point as predicted by the steady state theory and the wave speed of the ESPROSE.m solution.

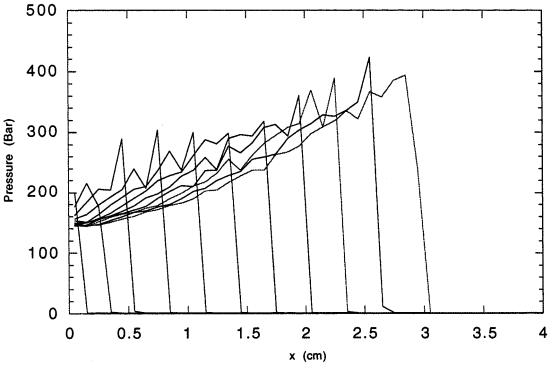

Fig. 35. The case of Fig. 31, run with the ESPROSE.m fragmentation model.

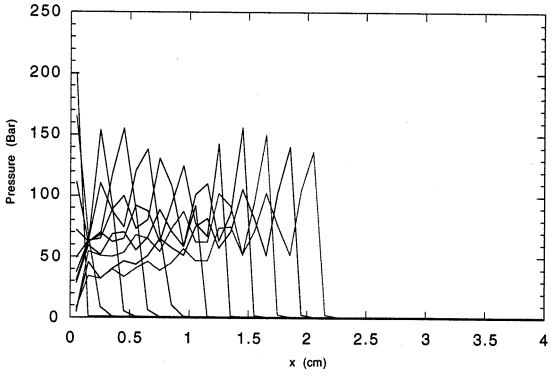

Fig. 36. The case of Fig. 31, run with the full ESPROSE.m microinteractions model.

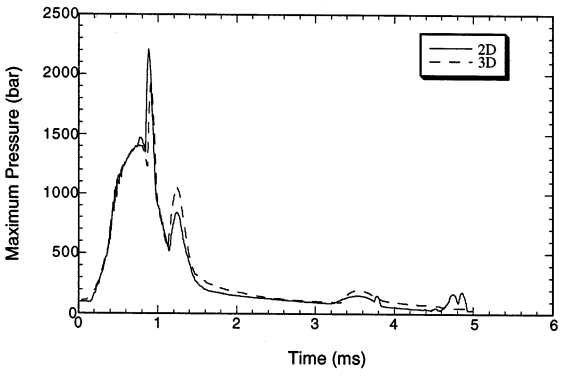

Fig. 37. Comparison between the peak pressures (anywhere, each time), obtained in the two codes with comparable input. The domain for the 3D code is an approximation of the axisymmetric case.

kinds of problems considered in this paper, it is clear that it can be controlled to an acceptable level. On this basis we made no special efforts toward further control, on the numerical front.

5.3. Artificial viscosity

It is well known that shock-capturing numerical schemes often require an artificial viscosity contribution to dampen numerically induced oscillations at the front. Our experience with ESPROSE.m is similar, and although not always needed, we have an artificial viscosity mechanism to control such oscillations when present. Some numerical experimentation is needed, if this is the case, because it is important not to overdamp the front. The numerous examples shown in this paper indicate that this can be done quite well.

6. Concluding remarks

In this verification effort, we have tried to test to the extent possible all key features of the numerical and physical aspects of the code. On the numerical side, we see no outstanding issue, but some improvements to enhance the code capability for very large geometries can be realized by implementing adaptive gridding. On the physical aspects also, we find no major outstanding issues. By a wide array of analytical and experimental tests we find that the wave dynamics are captured in an impressive manner, that the treatment of microinteractions is promising, and that this treatment is quite consistent with available data from integral explosions.

We can identify only one major need, and two areas for further improvements. The need is for expanding the microinteractions data base to reactor materials; that is, corium (ZrO_2/UO_2) melts. This will be done in the SIGMA-3000 facility currently nearing completion. We expect that these results will prove confirmatory of the energetics computed with the current constitutive laws for microinteractions in ESPROSE.m. We also expect that these results will clearly reveal the limitations, if any, of oxidic reactor materials to explode. This is needed if such limitations (presently suspected) are to be properly used in safety analyses. In the 'desirable improvements' (as opposed to 'needs') category, we would include a better knowledge of initial conditions of the premixtures in KROTOS-like experiments, and a better understanding of the local structure of the shock front, both experimentally and theoretically. This latter aspect involves the secondary structures of the pressure waves and its effect on the microinteractions, and a more basic starting point for the formulation of the constitutive laws for microinteractions.

To close, we would like to return to the essence of our basic approach: having the microinteractions under simulated large scale explosions, having consistent interpretations for well-characterized 1D propagations in the laboratory, and having established that the wave dynamics under multiphase multidimensional conditions can be adequately captured, provides for an efficient and robust basis for meeting the practical goal of steam explosion research, i.e. predicting the magnitude of energetics for large scale explosions under conditions of practical interest. Most importantly, this approach obviates the need for very large scale multidimensional explosion experiments.

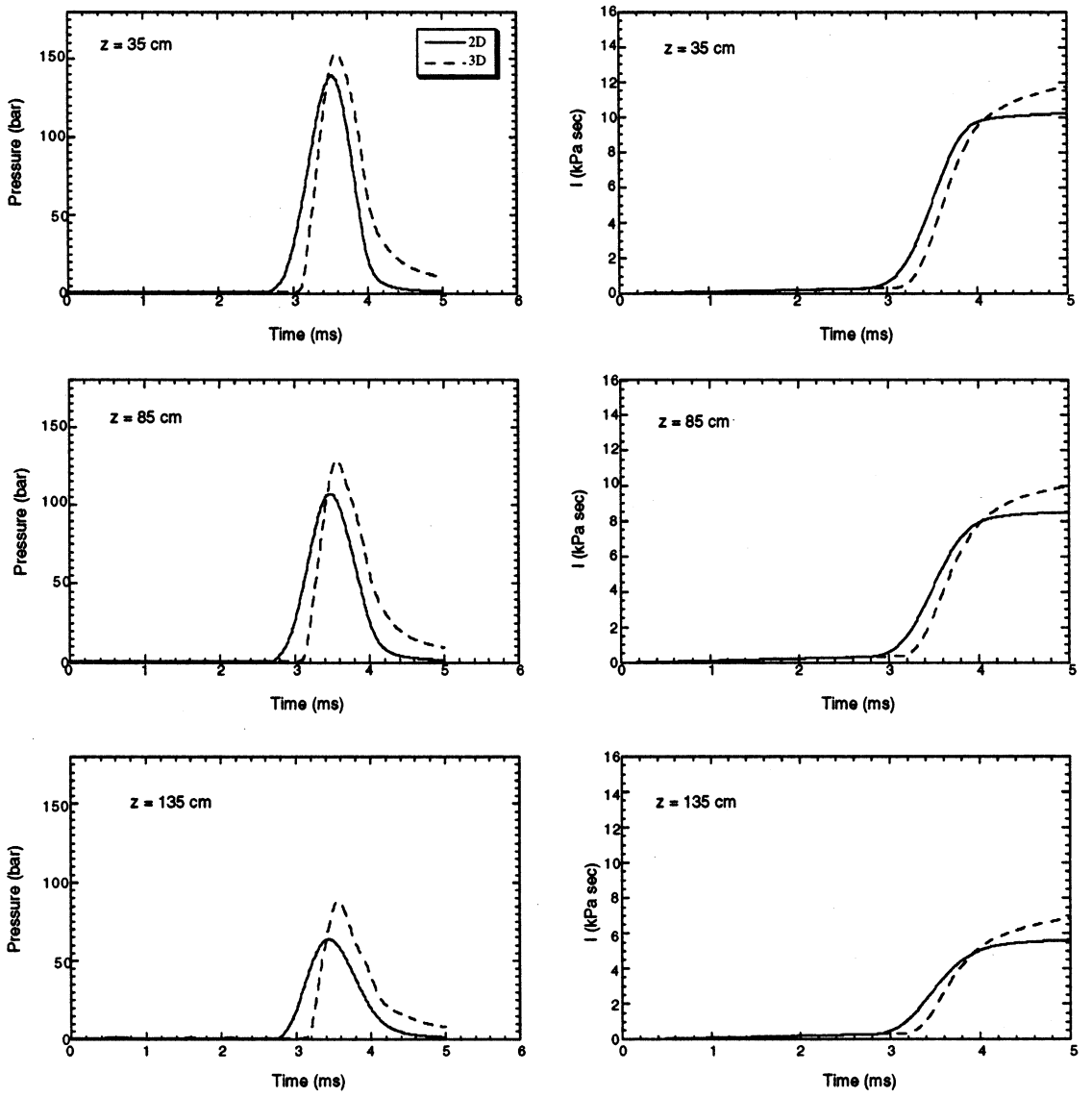

Fig. 38. Pressure pulses and impulse loadings at the boundaries for the explosion of Fig. 37. The position heights indicated (z) are from the bottom of the pool.

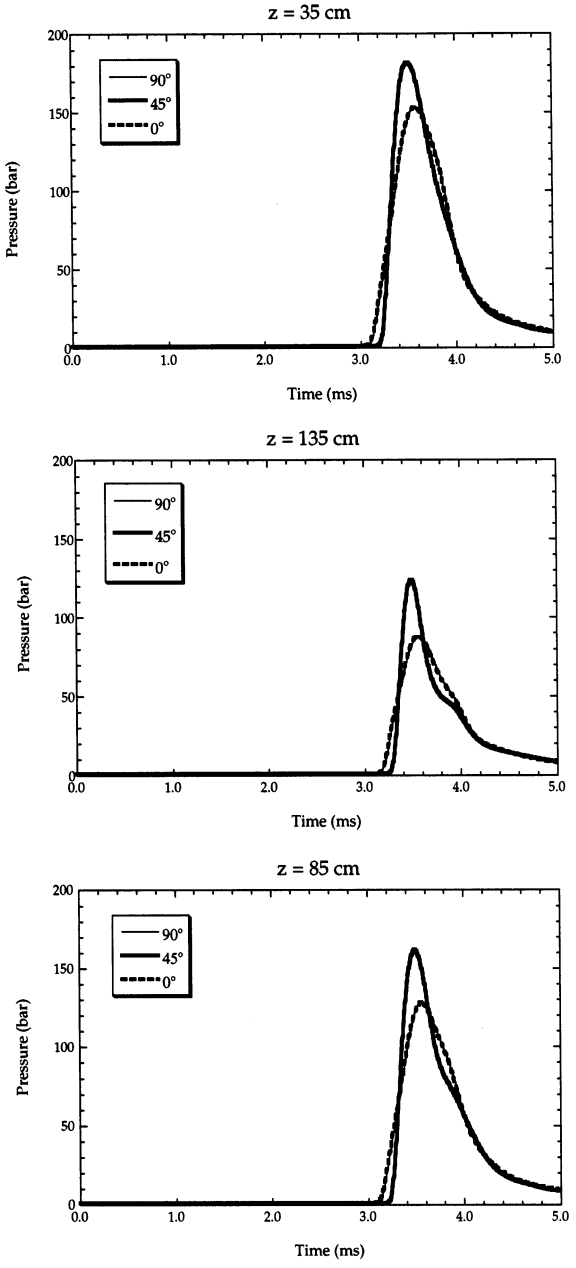

Fig. 39. Check of axisymmetry for the 3D code, under the explosion of Fig. 37. The x and y (0°, 90°) axis results in effect coincide.

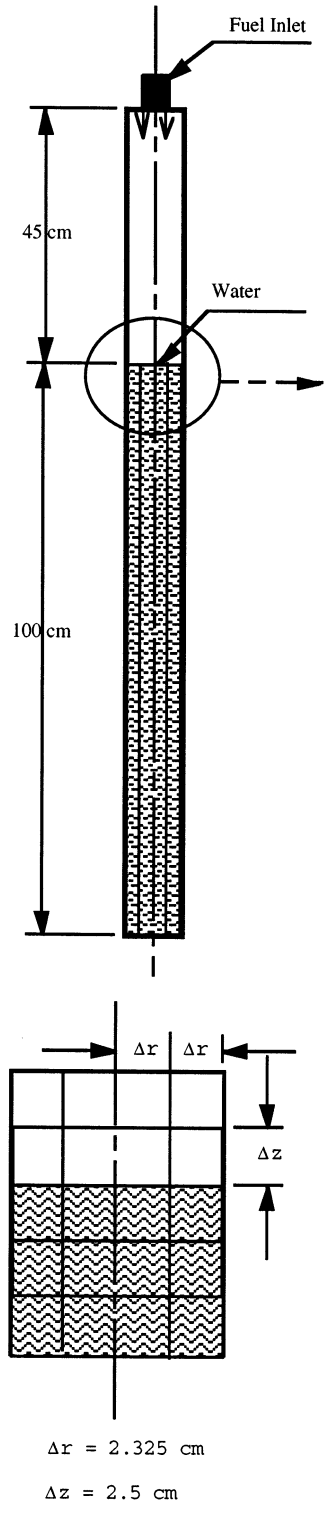

Fig. 40. The discretization of the KROTOS vessel used in PM-ALPHA.L-3D, and ESPROSE.m-3D. The cross-sectional area is preserved.

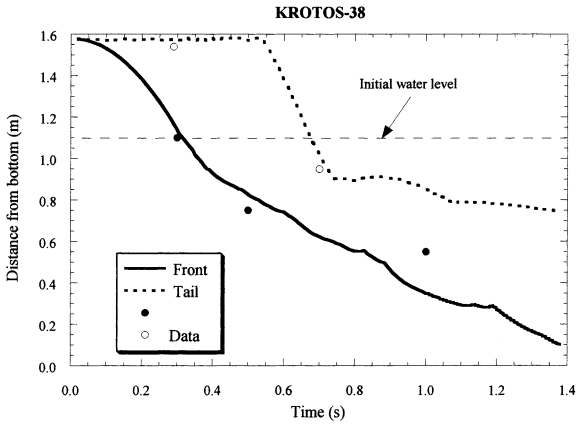

Fig. 41. The front advancement predicted by PM-ALPHA against the thermocouple 'indications' of the front in test K38. Open circles probably indicate delayed 'hits.'

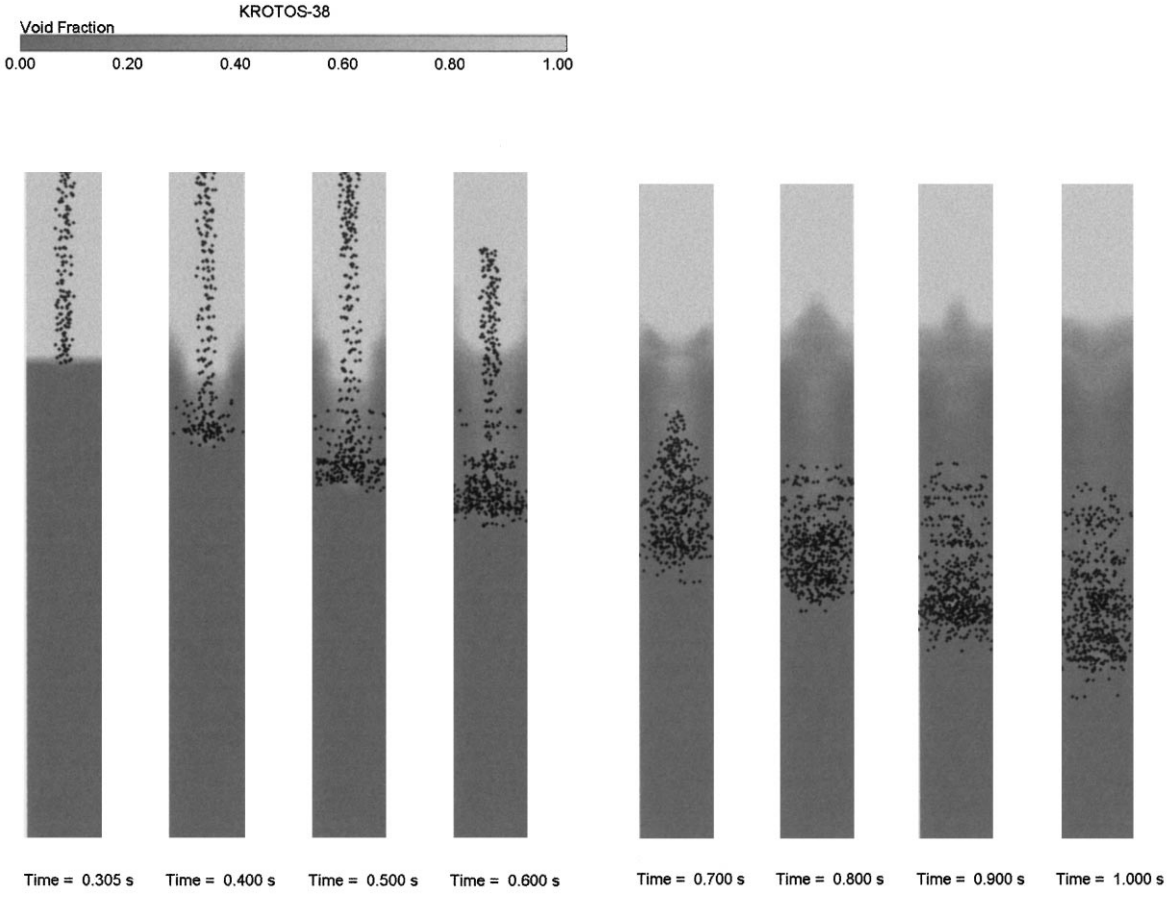

Fig. 42. Premixing maps of the PM-ALPHA.L simulation of K38.

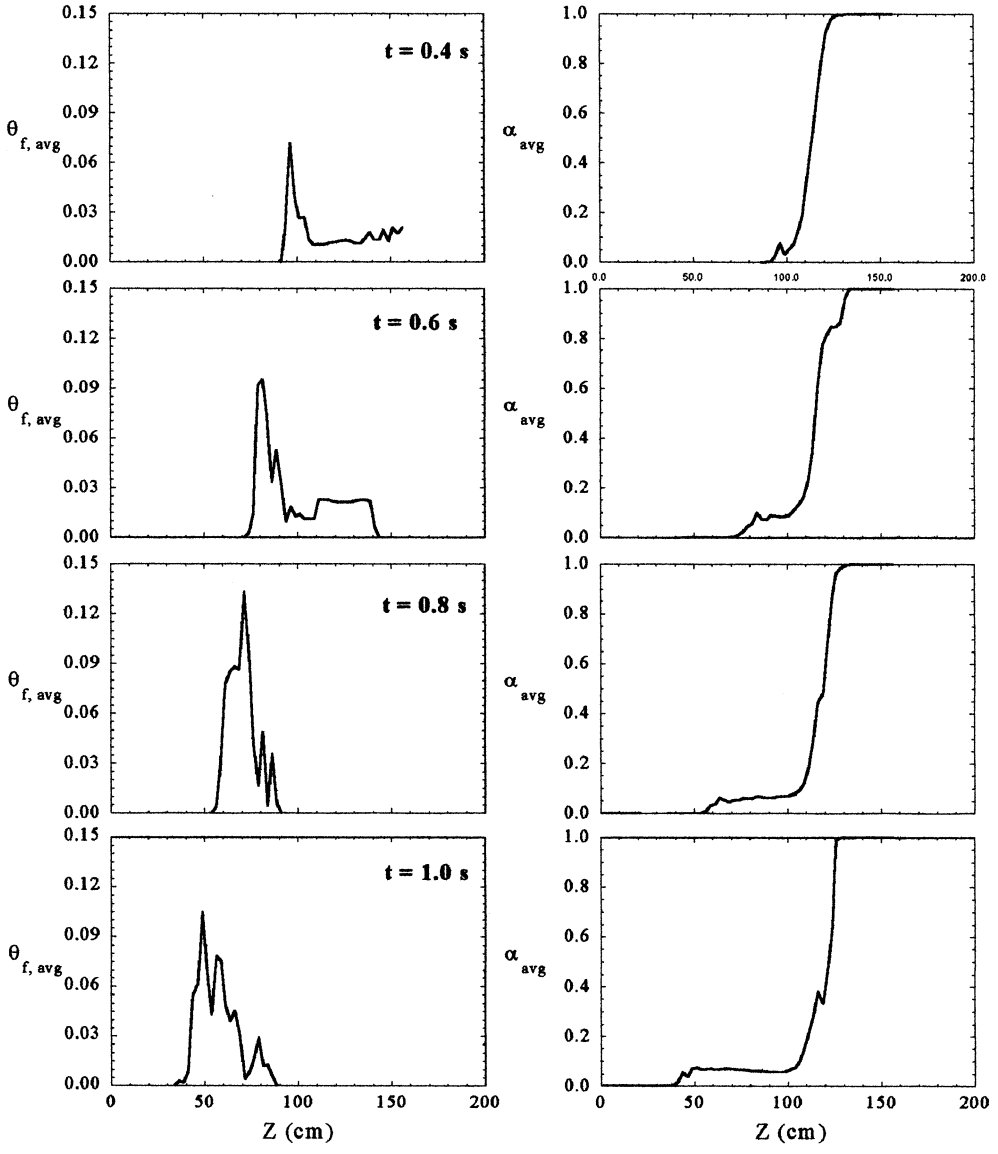

Fig. 43. The predicted area-averaged fuel volume fraction and steam void fraction transients in K38.

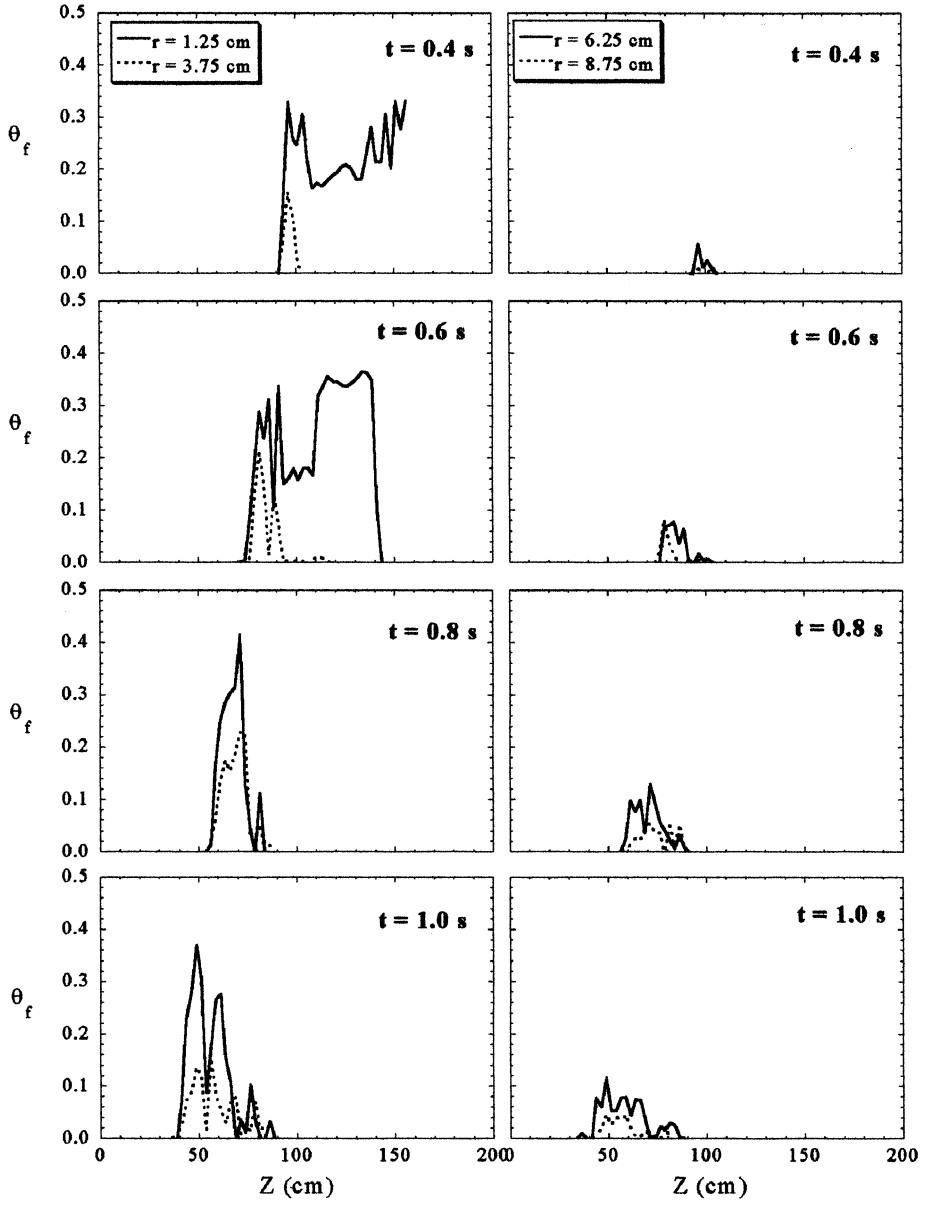

Fig. 44. The predicted fuel volume fraction in the two inner cells and two outer cells for K38.

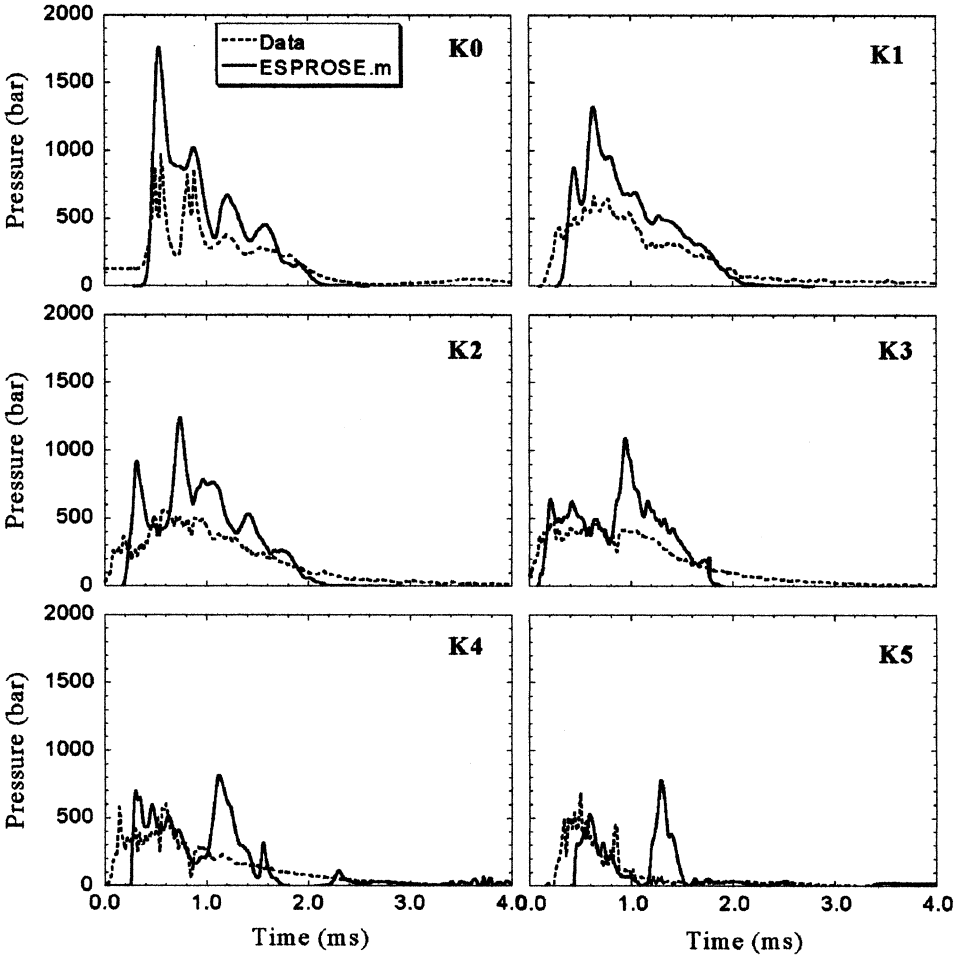

Fig. 45. The explosion predicted by ESPROSE.m against the data of K38. The microinteractions parameters are $\beta_f = 9$ and $f_e = 7$.

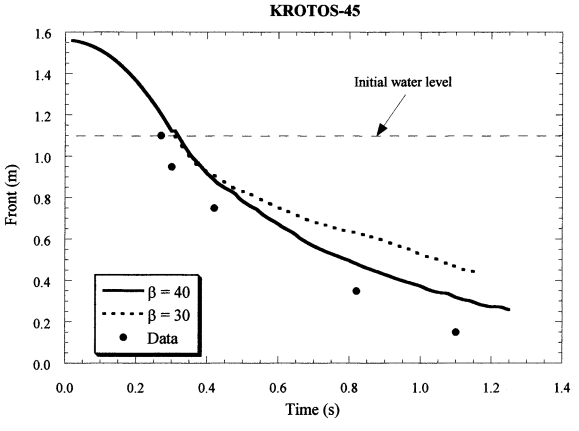

Fig. 46. The front advancement predicted by PM-ALPHA.L against the thermocouple 'indications' of the front for test K45.

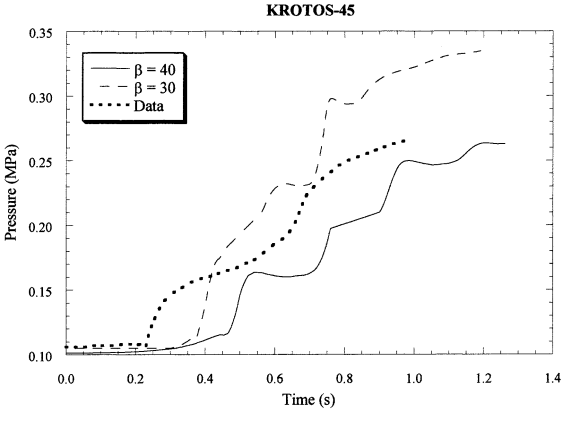

Fig. 47. The pressurization predicted by PM-ALPHA.L against experimental data.

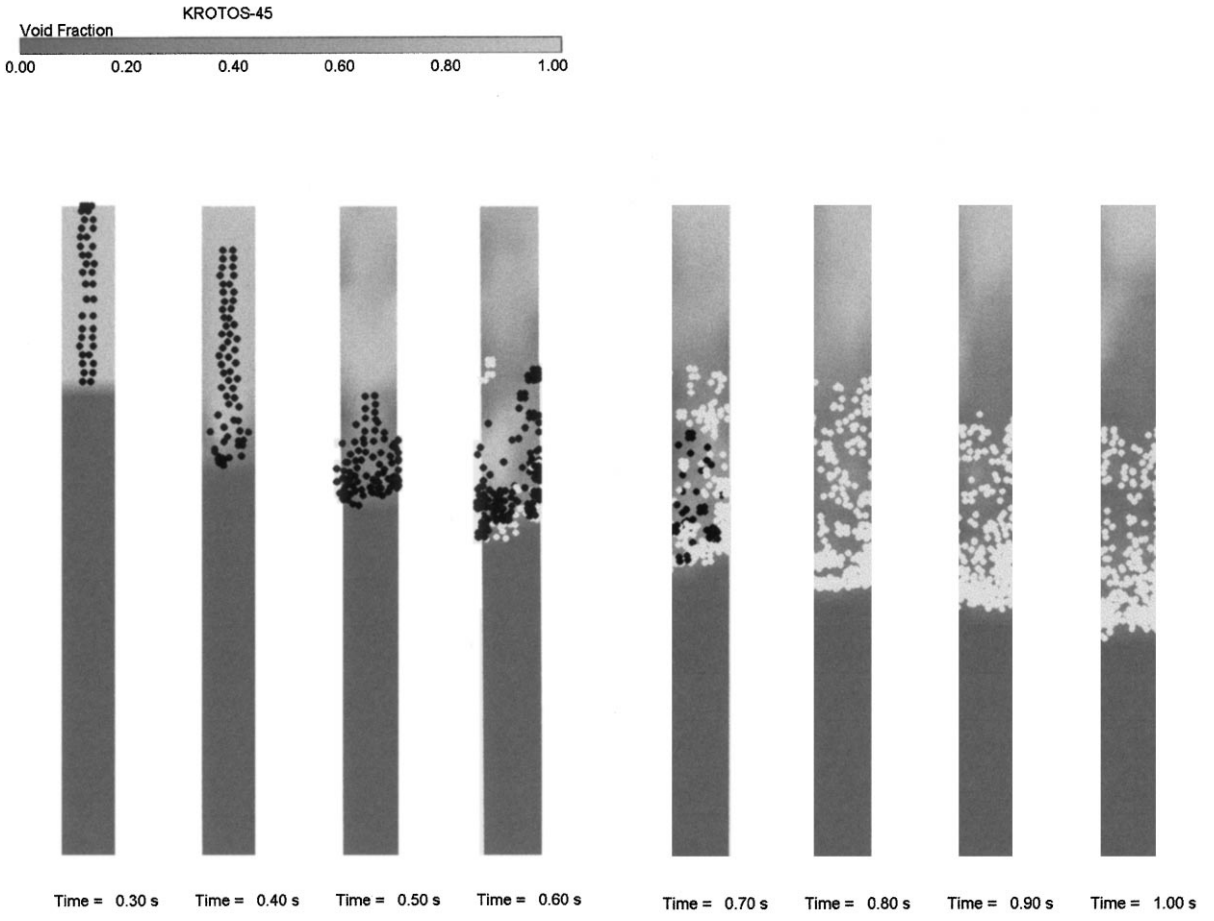

Fig. 48. Premixing maps of the PM-ALPHA.L simulation of K-45 (with $\beta = 30$). White fuel particles are more than 50% frozen.

Acknowledgements

This work was supported under the ROAAM program carried out for the US DOE's Advanced Reactor Severe Accident Program (ARSAP), under ANL subcontract No. 23572401 to UCSB.

References

Chen, X., Yuen, W.W., Theofanous, T.G., 1995. On the constitutive description of the microinteractions concept in steam explosions, in: NURETH-7, Saratoga Springs, NY, September 10–15, NUREG/CP-0142, Vol. 1, 1586–1606

Chen, X., Luo, R., Yuen, W.W., Theofanous, T.G., 1997. Experimental simulation of microinteractions in large scale explosions, in: OECD/CSNI Specialist Meeting on Fuel–Coolant Interactions, Jaeri, Tokyo, Japan, May 19–21, NEA/CSNI/R(97)26, pp. 364–389 (also in this issue).

Hibbit, H.D., et al., 1994. ABAQUS Version 5.3.

Huhtiniemi, I., Hohmann, H., Magallon, D., 1995. FCI experiments in the corium/water system, in: Proceedings of the 7th International Meeting on Nuclear Reactor Thermal-Hydraulics NURETH-7, Saratoga Springs, NY, September 10–15, NUREG/CP-0142, pp. 1712–1727.

James, R.J., 1989. ANACAP-3D—Three-dimensional analysis of concrete structures: theory, user's and verification manuals, ANATECH No. ANA-89-0094. Anatech Research Corporation report for Anatech Research Corporation, San Diego, CA, USA.

Landau, L.D., Lifshitz, E.M., 1959. Fluid Mechanics. Addison-Wesley, Reading, MA.

Moody, F.J., 1990. Introduction to Unsteady Thermofluid Mechanics, Section 2. Wiley, New York.

Theofanous, T.G., Yuen, W.W., 1994. The prediction of dynamic loads from ex-vessel steam explosions, in: Proceedings, International Conference, New Trends in Nuclear System Thermohydraulics, Pisa, May 30–June 2, pp. 257–270.

Theofanous, T.G., Yuen, W.W., Sienicki, J.J., Chu, C.C., The probability of a reactor pressure vessel failure by steam explosions in an AP600-like design, DOE/ID-10505. Actually issued as DOE/ID-10541 under the title: 'Lower head integrity under in-vessel steam explosion loads,' Theofanous, T.G., Yuen, W.W., Angelini, S., Sienicki, J.J., Freeman, M., Chen, X., Salmassi, T. June 1998, vol 1 + 2. US Department of Energy Draft Report; not published as the SWR was discontinued.

Theofanous, T.G., Yuen, W.W., Sienicki, J.J., Chu, C.C., The probability of containment failure by steam explosions in an SBWR-like lower drywell, DOE/ID-10506. US Department of Energy Draft Report; later issued under a different title on US Department of Energy Report, DOE/ID-10541, June 1998, vol. 1 and vol. 2

Theofanous, T.G., Yuen, W.W., Angelini, S., Chen, X., 1995a. The Study of Steam Explosions in Nuclear Systems, DOE/ID-10489, January. US Department of Energy Report

Theofanous, T.G., Yuen, W.W., Freeman, K., Chen, X., 1995b. Escalation and propagation of steam explosions: ESPROSE.m verification studies, DOE/ID-10503, August. US Department of Energy Report

Theofanous, T.G., Angelini, S., Yuen, W.W., 1995c. Premixing of steam explosions: PM-ALPHA verification studies, DOE/ID-10504, September. US Department of Energy Report

Theofanous, T.G., 1996. On the proper formulation of safety goals and assessment of safety margins for rare and high-consequence hazards. Reliab. Eng. Syst. Saf. 54, 243–257.

THIRMAL-1, 1993. Computer code for analysis of interactions between a stream of molten corium and a water pool. Vol. 1: Code Manual, EPRI TR-103417-V1, Project 3130-01, Final Report (December). Vol. 2: User's Manual, EPRI TR-103417-V2, Project 3130-01, Final Report (December).

Yuen, W.W., Theofanous, T.G., 1995a. ESPROSE.m: A computer code to stimulate the transient behavior of a steam explosion based on the microinteractions concept, Department of Energy Report, DOE/ID-10501, April.

Yuen, W.W., Theofanous, T.G., 1995b. PM-ALPHA: A computer code for assessing the premixing of steam explosions, DOE/ID-10502, April.

Yuen, W.W., Theofanous, T.G., 1997. On the existence of multiphase thermal detonations, in: International Seminar on Vapor Explosions and Explosive Eruptions (AMIGO-IMI), Sendai, Japan, May 22–24, pp. 3–10.